









Global Structure of Magnetotail Reconnection Revealed by Mining Space Magnetometer Data

G. K. Stephens¹ , M. I. Sitnov¹ , R. S. Weigel² , D. L. Turner¹ , N. A. Tsyganenko³ ,
A. J. Rogers^{4,5} , K. J. Genestreti⁶ , and J. A. Slavin⁷ 

¹The Johns Hopkins University Applied Physics Laboratory, Laurel, MD, USA, ²George Mason University, Fairfax, VA, USA, ³Saint-Petersburg State University, Saint-Petersburg, Russia, ⁴University of New Hampshire, Durham, NH, USA, ⁵Los Alamos National Laboratory, Los Alamos, NM, USA, ⁶Space Science and Engineering, Southwest Research Institute, Durham, NH, USA, ⁷Department of Climate and Space Sciences and Engineering, University of Michigan, Ann Arbor, MI, USA

Key Points:

- Global structure of magnetotail reconnection inferred from data mining matches its locations revealed by in situ observations
- Reconstructed magnetotail reconnection structures include X- and O-lines and magnetic nulls
- Reconstructed multiscale current sheet structure is consistent with its formation mechanism by quasi-adiabatic ion motions

Supporting Information:

Supporting Information may be found in the online version of this article.

Correspondence to:

G. K. Stephens,
Grant.Stephens@jhuapl.edu

Citation:

Stephens, G. K., Sitnov, M. I., Weigel, R. S., Turner, D. L., Tsyganenko, N. A., Rogers, A. J., et al. (2023). Global structure of magnetotail reconnection revealed by mining space magnetometer data. *Journal of Geophysical Research: Space Physics*, 128, e2022JA031066. <https://doi.org/10.1029/2022JA031066>

Received 11 OCT 2022
Accepted 9 JAN 2023

Author Contributions:

Conceptualization: G. K. Stephens, M. I. Sitnov, N. A. Tsyganenko, A. J. Rogers, K. J. Genestreti
Data curation: G. K. Stephens
Formal analysis: G. K. Stephens
Funding acquisition: M. I. Sitnov
Investigation: G. K. Stephens
Methodology: G. K. Stephens, M. I. Sitnov, N. A. Tsyganenko
Project Administration: M. I. Sitnov
Software: G. K. Stephens, M. I. Sitnov, N. A. Tsyganenko
Supervision: M. I. Sitnov, R. S. Weigel
Validation: G. K. Stephens, M. I. Sitnov
Visualization: G. K. Stephens
Writing – original draft: G. K. Stephens, M. I. Sitnov
Writing – review & editing: G. K. Stephens, M. I. Sitnov, R. S. Weigel, D. L. Turner, N. A. Tsyganenko, J. A. Slavin

Abstract Reconnection in the magnetotail occurs along so-called X-lines, where magnetic field lines tear and detach from plasma on microscopic spatial scales (comparable to particle gyroradii). In 2017–2020, the Magnetospheric MultiScale (MMS) mission detected X-lines in the magnetotail enabling their investigation on local scales. However, the global structure and evolution of these X-lines, critical for understanding their formation and total energy conversion mechanisms, remained virtually unknown because of the intrinsically local nature of observations and the extreme sparsity of concurrent data. Here, we show that mining a multi-mission archive of space magnetometer data collected over the last 26 yr and then fitting a magnetic field representation modeled using flexible basis-functions faithfully reconstructs the global pattern of X-lines; 24 of the 26 modeled X-lines match ($B_z = 0$ isocontours are within ~ 2 Earth radii or R_E) or nearly match ($B_z = 2$ nT isocontours are within $\sim 2R_E$) the locations of the MMS encountered reconnection sites. The obtained global reconnection picture is considered in the context of substorm activity, including conventional substorms and more complex events.

Plain Language Summary Magnetic reconnection is a fundamental process in plasmas which couples microscopic scales (\sim electron to proton gyroradii) to explosive macroscopic phenomena many orders of magnitude larger, such as solar flares and geomagnetic storms/substorms. Reconnection forms along “X-lines”, rifts where oppositely directed magnetic field lines are forced together. In the Earth’s magnetosphere, reconnection has been observed by satellites at isolated locations; however, the large-scale structure of X-lines and their time evolution remains unknown because of the rarity and local nature of observations. Here, ground based measurements of geomagnetic activity and solar wind measurements are used to data-mine 26 yr of magnetometer data from 22 Earth-orbiting satellites, which are then utilized to reconstruct the global magnetic field associated with X-lines in Earth’s magnetosphere. We show that these reconstructions pinpoint the reconnection locations by verifying their consistency with direct spacecraft observations.

1. Introduction

X-lines are one of the most fundamental structures in magnetized plasmas, particularly in space, where they link global or even astronomical scale processes to those on the single particle orbit scale, thereby allowing those microscale processes to shape the universe (Ji et al., 2022). Dungey (1961) suggested that the interaction between Earth’s magnetic dipole and the solar wind causes reconnection of magnetic field lines on both the day and nightsides of Earth’s magnetosphere. The shape of these reconnecting field lines resembles the letter “X” and extends tens of Earth radii ($R_E = 6,371.2$ km) in the dawn-dusk direction thus forming X-lines. An X-line divides space into four sectors. In one pair of opposing sectors, the magnetic field and plasma converge toward the center of the X while in the other pair, they are rapidly ejected from it. This reconnection process transforms energy stored in the magnetic field into particle kinetic and thermal energy, making it an efficient energy converter and particle accelerator (Ji et al., 2022). X-lines couple kinetic processes on proton and even electron gyroradius scales ($\lesssim 0.01R_E$) (Torbert et al., 2018) to space weather phenomena on global scales: such as solar flares, coronal mass ejections, and magnetospheric storms and substorms ($\sim 10R_E$) (Camporeale, 2019). This range of scales is so immense that its modeling has become one of the major challenges for nascent exascale computing (Ji et al., 2022).

While the microscale physics of reconnection in the magnetosphere has been studied in detail using recent multi-probe satellite missions (Angelopoulos et al., 2008; Burch, Moore, et al., 2016; Burch, Torbert, et al., 2016; Torbert et al., 2018), its global structure is difficult to infer from data due to their paucity (rarity and locality): at any moment the huge volume of the magnetosphere $\gtrsim 10^5 R_E^3$ is probed by less than a dozen spacecraft (Sitnov, Stephens, et al., 2019). Understanding the global structure of reconnection is fundamental for determining substorm triggering mechanisms (Sitnov, Birn, et al., 2019) and the total energy conversion during storms and substorms (Angelopoulos et al., 2020, 2013). Further, if X-line maps can be constructed from data, these maps could guide large-scale magnetohydrodynamic simulations of the magnetosphere by introducing a non-zero resistivity at their locations (Birn et al., 1996).

On the dayside, the X-line location can be readily estimated from the global geometry of the solar wind and Earth's magnetic fields along with other well-defined physical parameters (Fuselier et al., 2011). In contrast, nightside reconnection is much less understood. Here, the solar wind-magnetosphere interaction stretches the dipole field lines in the antisunward direction forming the magnetotail while storing energy in the magnetic field. The release of this stored energy via reconnection is often unsteady and spontaneous. Observations of substorms (Angelopoulos et al., 2008, 2013; Baker et al., 1996; Hones, 1984; McPherron et al., 1973; Russell & McPherron, 1973) suggest that new X-lines form in the tail at distances of 10–30 R_E and that this distance is controlled by the solar wind input (Nagai et al., 2005; Nagai & Shinohara, 2022). However, despite decades of debate and being the target of dedicated satellite missions (Angelopoulos et al., 2008; Burch, Moore, et al., 2016; Burch, Torbert, et al., 2016; Nagai et al., 2005), the factors that determine the emergence, location, size, and shape of nightside X-lines remain a major mystery in heliophysics.

The recent four-probe Magnetospheric MultiScale (MMS) mission (Burch, Moore, et al., 2016) enabled microscopic analysis of magnetotail reconnection down to electron gyroradius scales (Torbert et al., 2018). During 4 yr of MMS observations, 26 potential X-line encounters were found in the magnetotail (Rogers et al., 2019, 2023), where explosive reconnection causes substorms (Angelopoulos et al., 2020, 2008; Sitnov, Stephens, et al., 2019). They were detected in the form of Ion Diffusion Regions (IDRs) characterized by reversals of the North-South component of the magnetic field, B_z , and of the Sun-Earth component of the proton bulk flow velocity, v_x .

In this study, the global structure of magnetotail reconnection is derived from a large set of historic satellite magnetometer measurements using an advanced data mining (DM) approach combined with a flexible analytical model of the magnetospheric current systems. We show that our technique provides evidence justifying the global reconnection structure: the obtained contours delineating B_z reversals pass through most of the micro-scale IDRs observed by MMS (Section 3). We further discuss implications of the obtained magnetotail picture to the multi-scale structure of its current sheet (Section 3.2), and then describe its uncertainty and in situ validation errors (Section 4). We then discuss the global X-line structure in the context of substorm activity (Section 5). This includes the evolution of the magnetotail structure during a particular substorm event and some unusual substorm effects. The results are summarized in Section 6. Throughout this study, vector quantities are represented in the Geocentric Solar Magnetospheric System (GSM).

2. DM Solution of the Data Paucity Problem

The key to solving the data paucity problem lies in the recurrent nature and repeatable pattern of storms and substorms. The storm recurrence time for medium intensity storms is approximately 2 weeks (Reyes et al., 2021), while it is 2–4 hr for periodic substorms (Borovsky & Yakymenko, 2017). This repeatability allows the magnetic field to be reconstructed not only from observations at the moment of interest but also from records identified via mining the space magnetometer archive (Section 2.1) by searching for other times when the magnetosphere was in a similar global state. The magnetospheric state is characterized using geomagnetic indices (metrics of magnetic activity derived from networks of ground magnetometers) and solar wind conditions. Specifically, the magnetospheric state is defined using a 5D state-space vector, $\mathbf{G}(t) = (G_1, \dots, G_5)$, formed from the geomagnetic storm index (SMRc), substorm index (SML), their time derivatives, and the solar wind electric field parameter (vB_z^{IMF} ; where v is the solar wind speed and B_z^{IMF} is the North-South component of the Interplanetary Magnetic Field, IMF). The SMR and SML (SMRc is a pressure-corrected SMR [Tsyganenko et al., 2021]) indices are provided by the SuperMag project (Gjerloev, 2012) and represent variations of the ground-based magnetometer records from low/mid- and high-latitude stations respectively analogous to the Sym-H and AL indices used before

(Sitnov et al., 2008; Stephens et al., 2019). Further details on the magnetospheric state-space are provided in Section 2.2.

The DM algorithm employed is based on the k-nearest neighbor (kNN) classifier method (Sitnov et al., 2008; Wettschereck et al., 1997). To illustrate the algorithm, assume the magnetic field reconstruction, $\mathbf{B}(t)$, is sought for a query time $t = t^{(q)}$. This corresponds to a particular point in the 5D state-space, $\mathbf{G}^{(q)} = \mathbf{G}(t^{(q)})$. Surrounding this point will be other points, $\mathbf{G}^{(i)}$, in close proximity to it; that is, its nearest neighbors (NNs). Distances between points in state-space are computed using the Euclidean metric. These NNs identify a relatively small subset of data from a large magnetometer database that are then used to fit a magnetic field model, yielding $\mathbf{B}(t^{(q)})$. The specific choice of the number of NNs to use in the reconstruction, k_{NN} , is dictated by a balance between over- and under-fitting. Stephens and Sitnov (2021) found the optimal number to be $k_{\text{NN}} = 32,000$ for tail reconstructions of substorms, corresponding to $\sim 1\%$ of the total database. The resulting subset is composed of a very small number ($\sim 1\text{--}10$) of real (from the event of interest) but many ($\sim 10^5$) virtual (from other events) satellites. See Section 2.3 for a more detailed description.

The large number of virtual points enables new magnetic field architectures (Stephens et al., 2019; Tsyganenko & Sitnov, 2007), which differ from classical empirical models with custom-tailored modules (e.g., Tsyganenko & Sitnov, 2005) by utilizing regular basis function expansions for the major magnetospheric current systems, to be used for the reconstructions. In particular, all near-equatorial currents are approximated by two expansions representing general current distributions of thick and thin current sheets (TCS) with different thickness parameters D and D_{TCS} . The latter accounts for the formation of ion-scale TCS prior to substorm onset (Sergeev et al., 2011) as is further discussed in Section 2.4.

The solar wind plasma and IMF measurements were obtained from the NASA Space Physics Data Facility through OMNIWeb (https://omniweb.gsfc.nasa.gov/ow_min.html). OMNIWeb utilizes solar wind measurements from the ACE, Wind, IMP 8, and Geotail mission's magnetic field and plasma instruments applying a time delay to propagate them to the bow shock nose. The 5 min cadence OMNI products were used throughout this study, including the values for the solar wind velocity, flow pressure, and the IMF. The SML and SMR 1 min indices were downloaded from the SuperMAG webpage (<https://supermag.jhuapl.edu/indices>).

The methodology (DM algorithm and magnetic field architecture) presented here advances that of previous works, notably Stephens et al. (2019). The primary changes are: (a) an updated magnetometer archive, (b) replacing the Sym-H and AL indices by SMR and SML respectively, (c) distance-weighting of the NNs, (d) new spatial dependent TCS module, and (e) the “bowl-shaped” deformation for the equatorial current sheet. The remainder of this Sections 2.1–2.4 provides additional details on the above summary and is provided here for completeness.

2.1. Archive of Space Magnetometer Data

The heritage of the space magnetometer data used in this study dates to earlier empirical models of storms (Tsyganenko & Sitnov, 2007) and subsequent DM reconstructions (Sitnov et al., 2008). As the DM approach relies on knowledge of the solar wind plasma and IMF conditions, the start of the magnetometer archive (January 1995) was chosen to approximately coincide with the advent of continuous long-term L1 monitoring of the upstream solar wind which began in late 1994 with the launch of the Wind spacecraft. That archive (Tsyganenko & Sitnov, 2007) consisted of magnetic field observations from the IMP-8, Geotail, the Geosynchronous GOES-8, 9, 10, and 12 satellites, Cluster, and Polar missions. The time-resolution of the magnetometer data provided by the missions is often higher than is necessary for global scale reconstructions, so it is common practice to downsample the original data source to a regular cadence by time-averaging over multiple measurements (e.g., Tsyganenko, Andreeva, Kubyskhina, Sitnov, & Stephens, 2021). A decision must then be made for the frequency of the downsampled data. The archive from Sitnov et al. (2008) and Tsyganenko and Sitnov (2007) choose 15 min averaging cadence except for when spacecraft were located within $r < 5R_E$, in which the higher spacecraft velocities prompted for a 5 min data cadence. This archive is available at http://geo.phys.spbu.ru/~tsyganenko/data_sets.html.

The data archive from Tsyganenko and Sitnov (2007) was later augmented for the DM reconstructions of substorms by updating the Polar and Cluster data sets and by adding the THEMIS and Van Allen probes magnetometer data (Stephens et al., 2019). This expansion proved useful in populating the equatorial inner magnetosphere and near-tail region with data. In constructing this archive, the data from these four missions was averaged to a 5 min cadence, but when incorporated into the DM algorithm, it was downsampled to 15 min when the spacecraft

Table 1
The Archive of Space Magnetometer Data

Spacecraft	Number	Period	Cadence (min)
Cluster 1	756,822	2001–2015	5
Cluster 2	753,580	2001–2015	5
Cluster 3	748,084	2001–2015	5
Cluster 4	561,497	2001–2015	5
Geotail	133,107	1995–2005	15
Polar	844,212	1996–2006	5
IMP-8	10,177	1995–2000	15
GOES-8	233,674	1995–2003	15
GOES-9	84,951	1995–1998	15
GOES-10	213,295	1999–2005	15
GOES-12	79,569	2003–2005	15
THEMIS-A	702,043	2008–2015	5
THEMIS-B	78,523	2008–2011	5
THEMIS-C	115,459	2008–2011	5
THEMIS-D	702,388	2008–2015	5
THEMIS-E	711,441	2008–2015	5
Van Allen A	337,582	2012–2016	5
Van Allen B	337,610	2012–2016	5
MMS 1	312,040	2015–2020	5
MMS 2	312,050	2015–2020	5
MMS 3	311,349	2015–2020	5
MMS 4	310,219	2015–2020	5
Total	8,649,672	1995–2020	5/15

location was $r \geq 5R_E$ to be consistent with the earlier archive. This extended database (including the Tsyganenko & Sitnov, 2007 database) is available on the NASA Space Physics Data Facility: https://spdf.gsfc.nasa.gov/pub/data/aaa_special-purpose-datasets/empirical-magnetic-field-modeling-database-with-TS07D-coefficients/. This archive was again extended in subsequent substorm reconstructions by adding the available MMS data, which at that time had completed a full season sampling the midtail following the extension of the MMS apogee to $r \approx 25R_E$ (Sitnov, Stephens, et al., 2019; Stephens & Sitnov, 2021). The addition of MMS data proved useful in the reconstruction of the mid-tail region including the resolution of X-line features (Sitnov, Stephens, et al., 2019). For those substorm reconstructions, data beyond the primary apogee of the Geotail mission, $r = 31R_E$, was filtered. This was performed primarily to remove data points from the two THEMIS probes as they transitioned to the ARTEMIS orbit, as the inclusion of this distant data could produce anomalous results (Stephens et al., 2019).

In this study, the magnetometer data archive has again been updated. First, given the importance of the MMS data set to this particular investigation, it was extended through the end of the year 2020, now encompassing three full tail seasons. Further, in February 2019, the MMS apogee was raised from $r \approx 25R_E$ to $r \approx 29R_E$ (Williams et al., 2020), increasing the amount of data in this region. Second, the THEMIS, Cluster, Van Allen Probes, and MMS data sets were all downsampled to a universal 5 min cadence, instead of switching between 5 and 15 min based on spacecraft's radial distance. The motivation is that the previous substorm investigations demonstrated that the DM approach can indeed reconstruct changes in the magnetosphere on the scale approaching 5 min resolution (Sitnov, Stephens, et al., 2019; Stephens et al., 2019). The remaining spacecraft data sets (Geotail, IMP-8, and GOES satellites) retain the 15 min data cadence. The third is that the radial filter was increased from $31R_E$ to $36R_E$. Although, as Figure S1 in Supporting Information S1 indicates, the data between $31R_E$ and $36R_E$ is relatively sparse, its inclusion was found to help stabilize the reconstructions in the region $r \approx 25\text{--}31R_E$, which was of particular importance for this study. The result is an archive of

8,649,672 magnetometer data records spanning the years 1995–2020 and radial distance 1.5 to $36R_E$. The resulting spatial distribution of the records is shown in Figure S1 in Supporting Information S1 while the breakdown of each individual spacecraft's contribution to the archive is displayed in Table 1.

The general process for constructing these data sets is as follows. First, the magnetometer data is downloaded from either the mission webpage or a community resource such as the NASA Space Physics Data Facility. Any anomalous data records are removed. The contribution of the internal magnetic field is removed utilizing the International Geomagnetic Reference Field (IGRF model; Alken et al., 2021). Data collected when the spacecraft was outside the magnetopause is filtered by either visual determination of magnetopause crossings or by application of empirical magnetopause models (e.g., Shue et al., 1998). The resulting data are then downsampled to the requisite data cadence using boxcar averaging. As one approaches the surface of the Earth, the magnitude of the background magnetic field, $|\mathbf{B}_{\text{int}}|$, becomes very large relative to the magnetic field generated by external current sources, $|\mathbf{B}_{\text{ext}}|$. Thus, distinguishing the external and internal fields requires attitude knowledge beyond the capacity of many spacecraft missions. For these reasons data is excluded when $r < 1.5R_E$ for equatorial orbiting spacecraft. For polar orbiting spacecraft (Polar and Cluster), a larger exclusion radius of $r < 3.2R_E$ was used to prevent the large magnetic field deviations due to low-altitude FACs from biasing the fit.

2.2. Storm-Substorm-Solar Wind State-Space

Storms and substorms and their response to solar wind drivers have a tendency to develop in repeatable and predictable ways as indicated by their manifestation in geomagnetic indices (e.g., Liemohn et al., 2018). This makes their empirical reconstruction using DM possible. To do this, the storm/substorm state of the magnetosphere is assumed to be characterizable using a low-dimensional state-space (Vassiliadis, 2006). For example,

earlier storm studies formulated a 3D state-space based on the storm-time index Sym-H, its time derivative, and the solar wind electric field parameter vB_z^{IMF} (Sitnov et al., 2008; where v is the X component of the solar wind bulk velocity which is multiplied by the Z component of the IMF in GSM coordinates), the idea being that these three parameters are representative of the storm-state of the magnetosphere (Burton et al., 1975; Vassiliadis et al., 1999). At any given moment in time, the storm-state of the magnetosphere is represented as a state-vector, $\mathbf{G}(t)$, within this state-space. As the storm develops, it will plot a trajectory through this state-space and similar events will trace similar trajectories. Subsequent substorm investigations expanded to a 5D state-space by adding the substorm index AL along with its time derivative (Stephens et al., 2019). For this study, the AL and Sym-H indices have been replaced by their SuperMAG counterparts (Gjerloev, 2012), SML and SMR respectively (Newell & Gjerloev, 2011, 2012). The primary reason for this change was that, as of the writing of this study, the digital values for the AL index are not available beyond March 2018. This would have nullified the expansion of the MMS data set discussed in the previous section. Further, the SuperMAG indices are computed using a much larger number of ground magnetometer stations (on the order of ~ 100 instead of ~ 10 that are used for AL and Sym-H). In particular, the higher density and smaller gaps between stations allow the SML index to detect substorms that may be missed by the AL index (Newell & Gjerloev, 2011). As with the earlier studies, the storm index has been pressure corrected to remove magnetic perturbations caused by the compression of the magnetopause (Gonzalez et al., 1994). The pressure corrected index, SMRC, is defined: $SMRC = 0.8 \cdot SMR - 13\sqrt{P_{dyn}}$ (Tsyganenko et al., 2021). The 5D storm/substorm state-space used here is defined:

$$G_1(t) = \langle SMRC \rangle \propto \int_{-\Pi_{st}/2}^0 SMRC(t + \tau) \cos(\pi\tau/\Pi_{st}) d\tau \quad (1)$$

$$G_2(t) = D\langle SMRC \rangle / Dt \propto \int_{-\Pi_{st}/2}^0 SMRC(t + \tau) \cos(2\pi\tau/\Pi_{st}) d\tau \quad (2)$$

$$G_3(t) = \langle SML \rangle \propto \int_{-\Pi_{sst}/2}^0 SML(t + \tau) \cos(\pi\tau/\Pi_{sst}) d\tau \quad (3)$$

$$G_4(t) = D\langle SML \rangle / Dt \propto \int_{-\Pi_{sst}/2}^0 SML(t + \tau) \cos(2\pi\tau/\Pi_{sst}) d\tau \quad (4)$$

$$G_5(t) = \langle vB_s^{IMF} \rangle \propto \int_0^{\tau_\infty} vB_s^{IMF}(t - \tau_\infty + \tau) \exp[(\tau - \tau_\infty)/\tau_0] d\tau \quad (5)$$

The integration convolves the original time-series data with smoothing windows, indicated by the $\langle \dots \rangle$ notation. In the case of Equations 1 and 3, the windows are half cosines which act to smooth SMRC and SML over storm ($\Pi_{st}/2 = 6$ hr) and substorms scales ($\Pi_{sst}/2 = 1$ hr) respectively (Stephens et al., 2019). Meanwhile, their smoothed time derivatives, indicated by the $D\langle \dots \rangle / Dt$ notation, Equations 2 and 4, are defined using two half cosine masks as described in Sitnov et al. (2012). The fifth parameter, Equation 5, uses an exponential function to smooth over vB_s^{IMF} (where $B_s^{IMF} = -B_z^{IMF}$ when $B_z^{IMF} < 0$ and $B_s^{IMF} = 0$ otherwise). The exponential function not only acts as a smoothing window but also captures the loading of magnetic flux in the lobes during the substorm growth phase, thus, the e-folding time, $\tau_0 = 0.5$ hr, was set based on the typical duration of the growth phase (Partamies et al., 2013). Six e-foldings were used in the convolution, $\tau_\infty = 6\tau_0$. Note, the integration only occurs over past data, as indicated by the limits of integration in Equations 1–5, to prevent non-causal effects, that is, to prevent \mathbf{G} from reacting to changes that have not yet occurred.

$\mathbf{G}(t)$ is then discretized by sampling Equations 1–5 at a 5 min cadence spanning the years 1995–2020 (corresponding to the magnetometer archive time period). Thus, each 5 min moment corresponds to a particular point in state-space, $\mathbf{G}(t = t_i)$, for a total number of points $k_{SS} \approx 2.7 \times 10^6$. Note, k_{SS} does not generally equal the number of magnetometer records in the archive, $k_{DB} = 8.6 \times 10^6$ from Table 1, since each state-space point may correspond to zero, one, or many magnetometer records. The DM reconstructions also then operate on a 5 min cadence.

2.3. Mining Data Using kNN

Our approach resembles the kNN method of DM (Vassiliadis et al., 1995; Wettschereck et al., 1997), but also has important distinctions (Sitnov et al., 2008; Stephens et al., 2019). First, while the kNN subsets are first

identified in the state-space, the magnetic field reconstruction is performed in the real space using magnetometer observations that occurred during those k_{NN} moments. The choice of the number of k_{NN} must be ample enough to fit flexible magnetic field models with high degrees of freedom (Stephens et al., 2019; Tsyganenko & Sitnov, 2007) while at the same time sufficiently small, $1 \ll k_{NN} \ll k_{SS}$, as to provide adequate sensitivity to the storm and substorm phases. Second, the state-space includes the smoothed time derivatives of the activity indices to increase the sensitivity of the DM procedure to these phases and to capture memory effects of the magnetosphere as a dynamic system (Sitnov et al., 2001).

Consider a particular moment of interest, $t = t^{(q)}$, which corresponds to a query point in state-space $\mathbf{G}^{(q)} = \mathbf{G}(t^{(q)})$. The distance, $R_q^{(i)}$, between each other state-space point, $\mathbf{G}^{(i)}$, and $\mathbf{G}^{(q)}$ is then defined using the Euclidean distance metric:

$$R_q^{(i)} = \sqrt{\sum_{k=1}^5 (G_k^{(i)} - G_k^{(q)})^2 / \sigma_{G_k}^2}, \quad (6)$$

where each state-space component, G_k from Equations 1–5, is standardized by dividing by its standard deviation σ_{G_k} (computed over the entirety of the state-space). The k_{NN} closest points in state-space thus form the NN subset for $t = t^{(q)}$.

Since the number of state-space points, k_{SS} , is quite large, the number of our instance-based subset k_{NN} can also be made sufficiently large to use for the magnetic field reconstruction a sufficiently flexible model with many degrees of freedom, which is described in the next section. The specific value of $k_{NN} = 32,000$ ($\sim 1\%$ of k_{SS}) used in this study was found before to provide good validation results and resolve the spatial structure of the magnetic field and its evolution during substorms without overfitting (Sitnov, Stephens, et al., 2019; Stephens & Sitnov, 2021; Stephens et al., 2019). Recall, each NN corresponds to a particular moment, thus adjacent NNs form intervals in time when the magnetosphere was presumably in a similar state. Those time intervals are then used to extract a subset of magnetometer records from the archive (Table 1). The number of records in the magnetometer subset, S_{NN} , again is not generally equal to k_{NN} as it depends on the number of probes available at any NN moment. Typical values of S_{NN} for this study are $S_{NN} \approx 9 \times 10^4$.

The model architecture (Section 2.4) is then fit by minimizing the weighted RMS difference between the observed and modeled magnetic field vectors over the kNN subset:

$$M_{err}^{(NN)} = \sqrt{\sum_{j \in S_{NN}} \sum_{l=x,y,z} w_j w_{(0)}(r) [B_l^{(mod)}(\mathbf{r}^{(j)}) - B_l^{j,obs}]^2}, \quad (7)$$

where $B_l^{j,obs}$ is the magnetic field record from the kNN subset and $B_l^{(mod)}(\mathbf{r}^{(j)})$ is the value of the l th magnetic field component of the model evaluated at the spacecraft location of j th NN observation $\mathbf{r}^{(j)}$.

Note that the data points in the objective function Equation 7 are weighted by two factors, w_j and $w_{(0)}(r)$, with the latter acting to mitigate the inhomogeneity of magnetometer records in the real space, which is seen from Figure S1 in Supporting Information S1. In this weighting procedure, which is described in more detail in Tsyganenko and Sitnov (2007), the data is binned into $0.5R_E$ intervals of the geocentric distance r . Then the weight $w_{(0)}(r)$ is calculated as $\langle \Delta N \rangle / \max\{0.2\langle \Delta N \rangle, \Delta N_i\}$, where ΔN_i is the number of data points in the i th bin and $\langle \Delta N \rangle$ is the average number per bin over the entire set.

The other weighting, w_j , distance-weights each magnetometer record based on its corresponding NN's distance, $R_q^{(i)}$, to the query point, $\mathbf{G}^{(q)}$, in the state-space using a Gaussian function:

$$w_j = \exp\left[-\frac{1}{2} \left(\frac{R_q^{(j)}}{\sigma R_{NN}}\right)^2\right]. \quad (8)$$

R_{NN} is the radius of the NN sphere defined as the distance between the query point $\mathbf{G}^{(q)}$ and the furthest NN: $R_{NN} = \max\{R_q^{(i)}\}$. This weighting scheme gives higher weights to data points that are presumably more similar to the event of interest which also mitigates kNN's bias toward weaker events caused by the inhomogeneity of data in the state-space (Stephens et al., 2020). The specific value of the weighting parameter $\sigma = 0.3$ used in this study was found in earlier studies to improve the spatial reconstruction and avoid overfitting for the chosen value of k_{NN} .

2.4. Model Magnetic Field Architecture

The analytical description of the magnetospheric magnetic field used in this study is similar to that of earlier empirical reconstructions of substorms and is described in more detail in Stephens et al. (2019) (the only differences are the variable TCS structure and the adoption of the “bowl-shaped” deformation as discussed below). The total magnetospheric magnetic field, \mathbf{B}_{tot} , can be described as a summation of fields owing to individual current systems: $\mathbf{B}_{\text{tot}} = \mathbf{B}_{\text{int}} + \mathbf{B}_{\text{FAC}} + \mathbf{B}_{\text{eq}} + \mathbf{B}_{\text{MP}}$. The internal field, \mathbf{B}_{int} , generated by currents deep in the Earth's interior, is represented by the IGRF model (Alken et al., 2021). Of interest are the magnetic fields generated by currents flowing within geospace, termed the external field, \mathbf{B}_{ext} . Specifically here, assuming the magnetopause as a perfectly conducting layer, the set of current systems is limited to those flowing within the magnetopause, the field-aligned currents \mathbf{B}_{FAC} and equatorial currents \mathbf{B}_{eq} , and on the magnetopause \mathbf{B}_{MP} .

The building block for the equatorial current systems is the general magnetic vector potential solution of a current sheet, $\mathbf{A}_{\text{sheet}}$, as detailed by Tsyganenko and Sitnov (2007). Solved in cylindrical coordinates (ρ, ϕ, z) , the solution is composed of a Fourier series in ϕ and a Fourier-Bessel series in ρ , and the resulting magnetic field, $\mathbf{B}_{\text{sheet}} = \nabla \times \mathbf{A}_{\text{sheet}}$, is given by a basis function expansion having the form:

$$\mathbf{B}_{\text{sheet}}(\rho, \phi, z) = \sum_{n=1}^N a_{0n}^{(s)} \mathbf{B}_{0n}^{(s)} + \sum_{m=1}^M \sum_{n=1}^N (a_{mn}^{(o)} \mathbf{B}_{mn}^{(o)} + a_{mn}^{(e)} \mathbf{B}_{mn}^{(e)}), \quad (9)$$

where \mathbf{B}_{0n} , $\mathbf{B}_{mn}^{(o)}$, and $\mathbf{B}_{mn}^{(e)}$ are basis functions with axially symmetry, odd (sine), and even (cosine) symmetry respectively; while a_{mn} is the amplitude coefficients. Defining the magnetic field as the curl of a magnetic vector potential ensures a divergenceless magnetic field and allows for modifications to the current sheet structure discussed below.

Note, although this yields an arbitrary description in ρ and ϕ , its structure in z is rigidly defined to be an infinitely thin current sheet at $z = 0$. However, the Dirac delta profile of the current density in z can be broadened into a realistic finite distribution by performing the variable substitution $\zeta = \sqrt{z^2 + D^2}$, introducing the parameter D as the current sheet half-thickness. Note, the thickness parameter D need not be a constant but can take the form of a differentiable function $D = D(\rho, \phi)$.

A distinctive feature of the magnetotail is the formation of multiscale current sheets in the substorm growth phase with an ion-scale TCS embedded into a much thicker current sheet (Sergeev et al., 2011). In order to capture this feature, Stephens et al. (2019) used two such expansions to describe the equatorial field:

$$\mathbf{B}^{(eq)}(\rho, \phi, z) = \mathbf{B}^{(eq)}(\rho, \phi, z; D) + \mathbf{B}^{(eq)}(\rho, \phi, z; D_{\text{TCS}}), \quad (10)$$

where D_{TCS} is constrained to be $D_{\text{TCS}} < D$. Further studies (Sitnov, Stephens, et al., 2019; Stephens et al., 2019) confirmed the buildup of TCS in the growth phase of substorms and their decay during the expansion and recovery phases.

These earlier studies assumed a spatially constant TCS thickness, $D_{\text{TCS}} = \text{const}$, although it was allowed to vary in time (Stephens et al., 2019). Here, the embedded TCS structure has been further generalized to verify the possible physical mechanisms of the TCS formation. It can be explained (e.g., Sitnov et al., 2006) by figure-eight like Speiser (1965) proton orbits. If this is the case, the parameter D_{TCS} of the magnetic field model should depend on the distance ρ from the Earth because the Speiser orbit size, ρ_{Si} , is inversely proportional to the magnetic field outside the sheet, B_L , which itself depends on ρ (Wang et al., 2004). To take this effect into account, the TCS half-thickness from Equation 10 is represented by:

$$D_{\text{TCS}}(x, y) = \left(\alpha e^{-\beta \rho'} + D_0^{-1} \right)^{-1}, \quad \rho' = \sqrt{(x - x_0)^2 + y^2}. \quad (11)$$

This functional form of the TCS introduces four free parameters, α , β , D_0 , and x_0 . D_{TCS} asymptotically approaches a value of D_0 as ρ gets large and is constrained to be $D_0 < D$. The α parameter, which must be positively valued, shifts the curve along ρ , with small values, for example, $\alpha \approx 0.001$, resembling a constant curve $D_{\text{TCS}} = D_0$, while larger values move the curve to larger values of ρ . Meanwhile, the β parameter affects how gradually the curve approaches D_0 , with smaller/larger values corresponding to a more gradual/abrupt transition. The fourth parameter, x_0 , allows D_{TCS} to shift along the Sun-Earth line.

A further complication is that the equatorial current system rarely lies in a plane centered about $z = 0$. The Earth's dipole axis is not generally orthogonal to the direction of the solar wind flow. The angle that the dipole axis makes with the Z axis of the GSM coordinate system is the “dipole tilt angle”. Its non-zero value may cause bending and warping of the tail current sheet while changes in the IMF clock angle (the angle between geomagnetic north and the projection of the IMF vector onto the GSM Y - Z plane) may twist the current sheet (Tsyganenko et al., 2015; Tsyganenko & Fairfield, 2004). These effects can be accounted for by the application of the general deformation technique (Tsyganenko, 1998). Specifically, here the “bowl-shaped” deformation from Tsyganenko (2014) is used, introducing three additional free parameters which define the center of the current sheet; the hinging distance R_H , the warping parameter G , and the twisting parameter TW .

The values of M and N determine the number of azimuthal and radial expansions in Equation 9 respectively and thus the resolution of the equatorial currents in ϕ and ρ respectively. Here, as with previous substorm investigations (Stephens et al., 2019), $(M, N) = (6, 8)$ as this was determined a sufficient resolution to resolve current structure throughout the near and mid-tail without overfitting to data (Stephens & Sitnov, 2021). Further, as with the prior investigations, in order to account for potential dynamical pressure effects on the structure of equatorial currents, each of the amplitude coefficient terms in Equation 9 are made explicit functions of P_{dyn} : $a_{\alpha\beta}^{(\gamma)} = a_{0,\alpha\beta}^{(\gamma)} + a_{1,\alpha\beta}^{(\gamma)} \sqrt{P_{dyn}}$, doubling their number. The end result is a total of 416 amplitude coefficients which determine the spatial structure of the equatorial current sheet.

The FAC magnetic field, \mathbf{B}_{FAC} , module used in this study is identical to that of Stephens et al. (2019). The foundation of their analytical description is the radially flowing conical current systems developed in Tsyganenko (1991), which are then bent to follow approximately dipolar field lines using the general deformation technique which also accounts for the day-night asymmetry (Tsyganenko, 2002a). The azimuthal dependence of the conical currents utilizes a Fourier series, giving them flexibility to reconstruct the magnetic local time variations of the FACs but at the expense of having a very rigid latitudinal structure. In order to mimic expansion like flexibility in latitude, four such conical current systems are placed at overlapping latitudes. The first four Fourier terms are used for each of the four latitudinal varying conical currents resulting in a total of 16 linear amplitude coefficients that determine the FACs spatial structure. Global rescaling parameters were introduced to allow the FACs to shrink and grow in response to storm and substorm phases. Instead of allowing each of the four current systems to rescale independently, the two higher latitude systems were tied to one parameter κ_{R1} and the two lower to another κ_{R2} . The values of κ_{R1} and κ_{R2} were constrained so that they approximated the region-1 and region-2 current systems respectively. This formulation was shown to successfully reproduce the more complex spiral like FAC pattern observed in the AMPERE data (Sitnov et al., 2017).

Unlike the other external fields, in which the magnetic field sought is consistent with some conceptualization of a current system, the magnetopause magnetic field, \mathbf{B}_{MP} , does not attempt to represent a current. Instead, the domain of validity of the model is restricted to just inside the magnetopause current layer, where $\mathbf{j}_{MP} = 0$. Thus, \mathbf{B}_{MP} is irrotational and can be represented by a magnetic scalar potential, $\mathbf{B}_{MP} = -\nabla U$ and its formulation is simply the solution to Laplace's equation: $\nabla^2 U = 0$ (Tsyganenko, 2013). In this context, \mathbf{B}_{MP} is termed a shielding field in that it ensures the magnetosphere is closed, that is, that field lines do not cross the magnetopause. A closed magnetosphere is represented by the condition $\mathbf{B}_{tot} \cdot \mathbf{n}_S = 0$, where S is the modeled magnetopause boundary and \mathbf{n} is the normal to that surface. Here, as with previous studies, S is defined as the Shue magnetopause (Shue et al., 1998). In practice it is more tractable to represent \mathbf{B}_{MP} as a combination of shielding fields: $\mathbf{B}_{MP} = \mathbf{B}_{int}^{(sh)} + \mathbf{B}_{FAC}^{(sh)} + \mathbf{B}_{eq}^{(sh)}$, that way, each shielding field can be formulated independently using a coordinate system and geometry that makes sense for that particular system. For example, owing to the cylindrical geometry of \mathbf{B}_{eq} , U_{eq} is represented by an expansion of Fourier-Bessel harmonics (Equation 20 of Tsyganenko & Sitnov, 2007), while U_{int} and U_{FAC} utilize an expansion of “Box” harmonics, appendix of Tsyganenko (1998) and Equation 34 of Tsyganenko (1995) respectively. The coefficients of the shielding field expansion are found by minimizing the normal component of the combined field at the magnetopause boundary, for example, $\min[(\mathbf{B}_{eq,j} + \mathbf{B}_{eq,j}^{(sh)}) \cdot \mathbf{n}_j]$. For a more thorough discussion on this topic see Tsyganenko (2013).

One more consideration built into the structure of the model is the magnetosphere's expansion and contraction in response to changes in the solar wind dynamical pressure, P_{dyn} . It is well established from observations of magnetopause crossings that the magnetopause responds to decreases/increases in P_{dyn} by expanding/contracting in a self-similar way, that is, its size changes but not its shape (e.g., Shue et al., 1998; Sibeck et al., 1991). This self-similarity is easily represented by rescaling the position vector as a function of P_{dyn} . Using simple

pressure balance considerations the functional form of this rescaling is $\mathbf{r}' = P_{dyn}^{-\kappa} \mathbf{r}$, where $\kappa = 1/6$ for a perfect dipole (Mead & Beard, 1964). Here, as with many previous empirical studies, all current systems are assumed to possess the same self-similarity rescaling, that is they all take the same functional form and same value of κ (Tsyganenko, 2013). This assumption simplifies the shielding of these fields as both the shielded and the shielding fields rescale together. κ could be treated as a free parameter when the model is fit to data, however, previous studies have shown κ to be relatively stable (Tsyganenko, 2002b), so here a constant value of $\kappa = 0.155$ from Tsyganenko and Sitnov (2007) was used.

To summarize, the final magnetic field model configuration includes 432 linear amplitude coefficients and 10 free nonlinear parameters D , α , β , D_0 , x_0 , R_H , G , TW , κ_{R1} , and κ_{R2} which are determined by fitting them to the identified subset of magnetometer data. The linear coefficients are determined by applying the singular value decomposition pseudo-inversion method to the overdetermined linear least squares problem (Jackson, 1972; Press et al., 1992). The nonlinear parameters are found by embedding the linear solver within the Nelder-Mead downhill simplex algorithm (Nelder & Mead, 1965).

3. IDRs and Reconstructed Global Reconnection Structures

3.1. Reconnection Features in the Equatorial Plane

The main goal of the MMS mission (Burch, Moore, et al., 2016) was the detection and investigation of reconnection regions in the magnetosphere and its boundary. That goal was relatively easy to achieve at the magnetopause because of its regular structure (Fuselier et al., 2011) and in the magnetosheath due to multiple reconnection sites in its turbulent plasma volume (Phan et al., 2018). By contrast, only a handful of fortunate X-line encounters were detected/investigated in the magnetotail (Chen et al., 2019; Torbert et al., 2018). In this regard, the proposed DM reconstructions offer an attractive opportunity to explore the dynamics of magnetotail topology on a global scale, and its fidelity can be demonstrated by comparing our results with MMS observations. Magnetic reconnection can be directly observed if and when a spacecraft fortuitously flies through an IDR, as shown in Figure 1. A recent systematic survey of MMS plasma and field data in 2017 (Rogers et al., 2019) identified 12 such magnetotail IDRs, defined as correlated reversals of the proton bulk flow velocity, v_x , and the North-South magnetic field, B_z , as shown in Figure 1 inset, along with additional Hall magnetic and electric field signatures. That analysis was later extended to 2018–2020 for a total of 26 IDR events (Rogers et al., 2023) labeled here A–Z, “IDR alphabet”, listed in Table 2. The second column in the table lists the starting date and time of each IDR interval found in Rogers et al. (2023). Due to the 5 min cadence of our DM approach, the actual reconstructed times are rounded to the nearest 5 min as indicated in the third column.

The DM reconstruction of the magnetic field for event Y in the early expansion phase of the 5 August 2020 substorm (Figure 1) shows the formation of an X-line at $r \approx 23R_E$ in the tail within $\sim 1R_E$ from the corresponding IDR marked by the large green circle. This data-derived image of the X-line resembles sketches of solar flare arcades (e.g., Shiota et al., 2005) but with a fundamental advantage that it is backed by a quantitative description. The X-line appears on the dusk flank of the tail illustrated as the earthward part of the $B_z = 0$ isocontour in the equatorial plane (black line). It also corresponds to an earthward edge of a relatively long ($25R_E$) spiral structure, shown by the sample field lines that encircle the tailward part of the $B_z = 0$ isocontour and form a magnetic O-line.

The projection of the magnetic field at the center of the tail current sheet into the equatorial plane is displayed in Figure 2d showing that the $B_z = 0$ contour passes within $\sim 1R_E$ of the IDR observed by MMS. This success is remarkable given that only $\sim 0.03\%$ (32 of the 105,975) of the measurements used to reconstruct the magnetic field were taken from this event, with the other 99.97% coming from other similar events identified using the above described DM approach. The reconstructions of three other events (G, M, W) presented in Figure 2 also show the $B_z = 0$ contours pass within $\sim 1R_E$ of the observed IDRs. Closer examination shows that only events G, W, and Y are X-lines, whereas event M corresponds to an O-line. Indeed, since the microscale formation of the MMS tetrahedron cannot determine X-line motions using timing analysis (e.g., Eastwood et al., 2010), or by framing the X-lines by being tailward and earthward of them (Angelopoulos et al., 2008), it cannot distinguish whether they are X- or O-lines.

The fourth column of Table 2 specifies the computed distance, D_{0nT} , between each MMS observed IDR event and the reconstructed $B_z = 0$ nT contour (distance is found as the minimum radius of the 3D sphere originating from the MMS tetrahedron which crosses the corresponding $B_z = \text{const}$ contour). This demonstrates that the

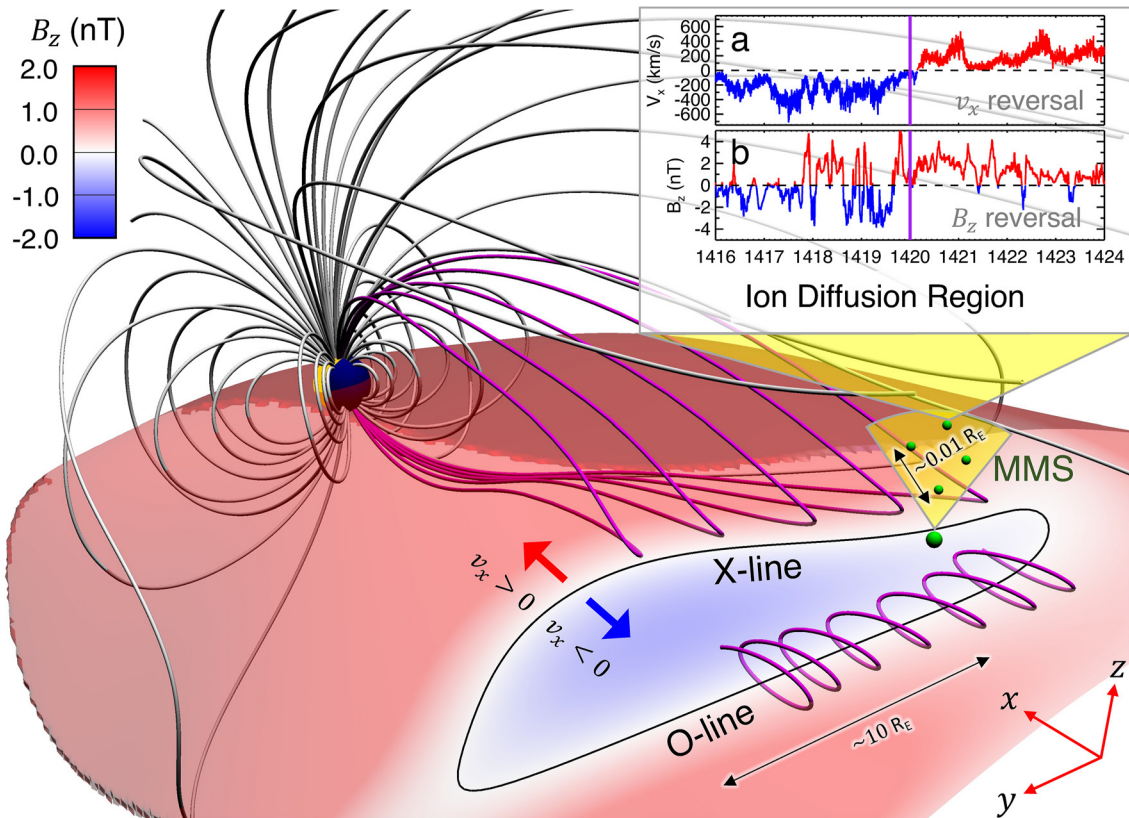


Figure 1. 3D global picture of the magnetosphere and local Magnetospheric MultiScale (MMS) observations for 5 August 2020 (event Y in Table 2) in GSM coordinates. It shows that the data mining reconstructed X-line matches one of 26 ion diffusion region (IDR) encounters observed by the MMS mission during 2017–2020. It includes selected field lines and the color-coded magnetic field distribution, B_z , sampled at the center of the tail current sheet taking into account deformation effects caused by the tilt angle of the Earth's dipole axis. The $B_z = 0$ isocontour is shown by the black line (the color table is saturated at $|B_z| = 2$ nT to better reveal the isocontour). The inset shows key IDR parameters: (a) the proton bulk flow velocity component v_x and (b) the magnetic field B_z , from the MMS4 probe (the small green spheres show the MMS tetrahedral configuration) whose location is marked by the larger green sphere near the equatorial plane. The purple vertical line marks the reconstruction moment, 5 August 2020, 14:20 UT. The 3D visualizations are constructed using the VisIt visualization tool (Childs et al., 2012).

consistency of the DM reconstructions are not isolated to just the events displayed in Figure 2. Indeed we can categorize 16 of our DM reconstructions as “Hits”, that is $D_{0nT} < 2.0R_E$, which includes 11 X-lines (A, C, D, E, G, Q, S, V, W, X, Y) and 5 O-lines (H, L, M, O, R). The equatorial X-line reconstructions for four of these events have been shown in Figure 2 while the analogous figures for the other 12 events are contained in the Supporting Information (Figures S2–S4 in Supporting Information S1).

Several more event reconstructions do not fully resolve the $B_z = 0$ nT contour in the vicinity of the observed IDR, but still resolve regions of small B_z near the IDR. To categorize these events, the distance, D_{2nT} , between the observed IDR and the $B_z = 2$ nT contour is displayed as the fifth column in Table 2. This yields 8 “Near Hits” (I, J, K, N, P, T, U, Z) where $D_{2nT} < 2.2R_E$ ($< 2R_E$ for all events except N). The equatorial B_z for these events are shown in Figures S5 and S6 in Supporting Information S1.

The two “Misses” (B, F) are then events where both $D_{0nT} \geq 2.0R_E$ and $D_{2nT} \geq 2.2R_E$ and are shown in Figure S7 in Supporting Information S1. However, both events have a plausible explanation. Event B occurs during weak magnetospheric activity (SML ≈ 0) with effectively no solar wind/IMF input ($vB_z^{IMF} > 0$) while event F takes place during the middle of a several hours long gap in solar wind and IMF data (they are interpolated in the reconstruction). The last column in Table 2 matches each IDR event to its corresponding figures.

3.2. Reconnection Features in the Meridional Planes

The corresponding meridional slices through the planes containing the IDRs of Figure 2 events (G, M, W, Y) are shown in Figure 3, illustrating the magnetic topology and distributions of electric currents, while the remainder of the IDR alphabet (Figures S2–S7 in Supporting Information S1) is shown in Figures S8–S13 in Supporting

Table 2
The Magnetospheric MultiScale Ion Diffusion Region Alphabet

Event	Start date/time	Model date/time	$D_{\text{onT}}(R_E)$	$D_{\text{2nT}}(R_E)$	Figures
A	2017-05-28T03:57	03:55	1.94	1.40	Figures S2 and S8 in Supporting Information S1
B	2017-07-03T05:26	05:25	4.72	3.23	Figures S7 and S13 in Supporting Information S1
C	2017-07-06T15:34	15:35	0.58	3.77	Figures S2 and S8 in Supporting Information S1
D	2017-07-06T15:45	15:45	1.72	2.54	Figures S2 and S8 in Supporting Information S1
E	2017-07-11T22:33	22:35	1.37	1.46	Figures S2 and S8 in Supporting Information S1
F	2017-07-17T07:48	07:50	8.62	5.78	Figures S7 and S13 in Supporting Information S1
G	2017-07-26T00:02	00:00	1.44	1.24	Figures 2 and 3
H	2017-07-26T07:00	07:00	1.91	1.63	Figures S3 and S9 in Supporting Information S1
I	2017-07-26T07:27	07:25	5.18	0.39	Figures S5 and S11 in Supporting Information S1
J	2017-08-06T05:13	05:15	7.70	0.63	Figures S5 and S11 in Supporting Information S1
K	2017-08-07T15:37	15:35	3.22	1.57	Figures S5 and S11 in Supporting Information S1
L	2017-08-23T17:53	17:55	1.88	0.54	Figures S3 and S9 in Supporting Information S1
M	2018-08-15T11:57	11:55	1.47	0.70	Figures 2 and 3
N	2018-08-26T06:38	06:40	2.85	2.17	Figures S5 and S11 in Supporting Information S1
O	2018-08-27T11:39	11:40	0.95	1.65	Figures S3 and S9 in Supporting Information S1
P	2018-08-27T12:14	12:15	7.43	1.19	Figures S6 and S12 in Supporting Information S1
Q	2018-09-10T17:14	17:15	0.78	1.02	Figures S3 and S9 in Supporting Information S1
R	2018-09-10T23:57	23:55	0.88	1.64	Figures S4 and S10 in Supporting Information S1
S	2019-07-25T21:40	21:40	1.45	4.26	Figures S4 and S10 in Supporting Information S1
T	2019-08-31T12:01	12:00	1.88	0.68	Figures S6 and S12 in Supporting Information S1
U	2019-09-06T04:38	04:40	3.57	0.77	Figures S6 and S12 in Supporting Information S1
V	2020-08-02T16:58	17:00	1.06	0.61	Figures S4 and S10 in Supporting Information S1
W	2020-08-02T17:09	17:10	0.65	0.55	Figures 2 and 3
X	2020-08-03T01:04	01:05	1.03	2.11	Figures S4 and S10 in Supporting Information S1
Y	2020-08-05T14:19	14:20	1.13	3.94	Figures 2 and 3
Z	2020-08-29T09:56	09:55	3.26	1.73	Figures S6 and S12 in Supporting Information S1

Information S1. The figures clarify that the observed $B_z = 0$ contours indeed represent X- and O-lines similar to the 3D magnetotail field geometry shown in Figure 1. They also confirm the quasi-2D nature of reconnection apparently imposed by the North-South symmetry of the magnetotail (e.g., Tsyganenko & Fairfield, 2004) which is drastically different from the inherently 3D reconnection processes in the solar corona (Liu et al., 2016) and rapidly rotating planets (Griton et al., 2018).

These meridional distributions resemble empirical visualizations of reconnection in laboratory plasmas, which became possible due to their large number of real probes (up to 200) and additional symmetry constraints, such as the cylindrical symmetry imposed by the toroidal-shaped flux cores in the PPPL Magnetic Reconnection Experiment (MRX; Ji et al., 2022). Still, in contrast to MRX, magnetotail reconnection is only quasi-2D due to the finite length of the X-line forming a closed loop with the O-line, as well as the explicit 3D effects, such as null-points (e.g., Greene, 1988; Ji et al., 2022). Null-points in the tail were indeed inferred from the four-probe Cluster observations (Xiao et al., 2006). They have also been extensively discussed as a key element of the substorm onset mechanism in global MHD simulations (Tanaka et al., 2021). An example of the null-point pair seen in our DM reconstruction of event Y is presented in Figure S14 in Supporting Information S1. Additional deviations from the simple 2D picture could be due to a strong IMF B_y (e.g., Cowley, 1981) or North-South oscillations of the tail current sheet that resemble a flapping flag (e.g., Sergeev et al., 2006; Sitnov, Birn, et al., 2019).

Another interesting feature of the meridional reconstructions, which has important physics implications, is evident in Figure 3. It shows the variable thickness of the TCS assumed by Equation 11 resulting in a gradually

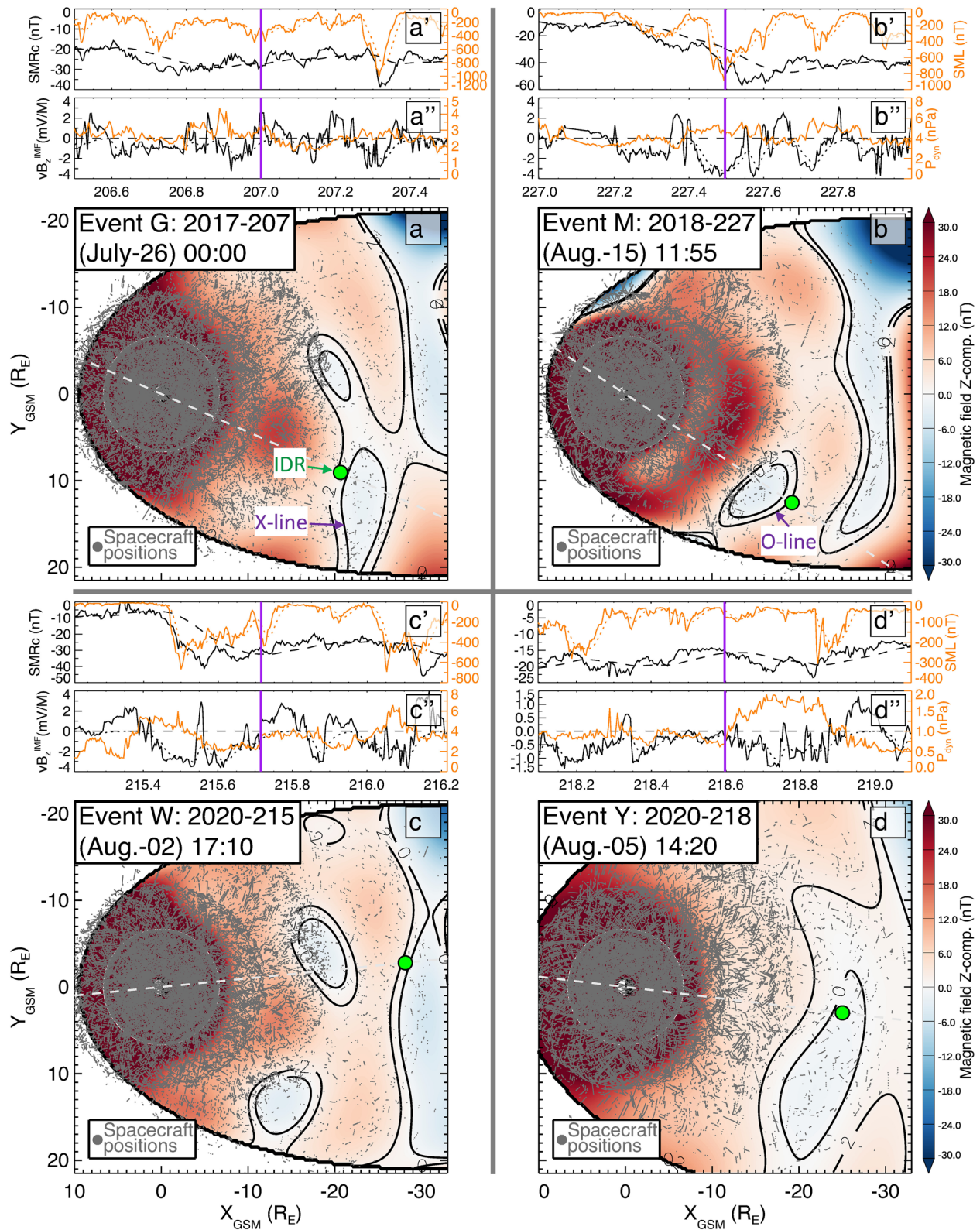


Figure 2. Ion Diffusion Regions (IDRs) and the equatorial magnetic field landscape. (a–d) Color-coded distributions of the equatorial magnetic field, B_z , with $B_z = 0$ and 2 nT isocontours (black lines), large green dots pointing to the IDRs, and gray dots showing the spacecraft positions for the nearest neighbor subsets used in the data mining method for four IDR events, G, M, W, and Y. Panels on top of each equatorial B_z distribution show the global context of the considered events in terms of (a'–d') the storm and substorm indices SMRc (black), SML (orange), and (a''–d'') the solar wind/IMF parameters vB_z^{IMF} (black) and P_{dyn} (orange) with the purple vertical line marking the event time.

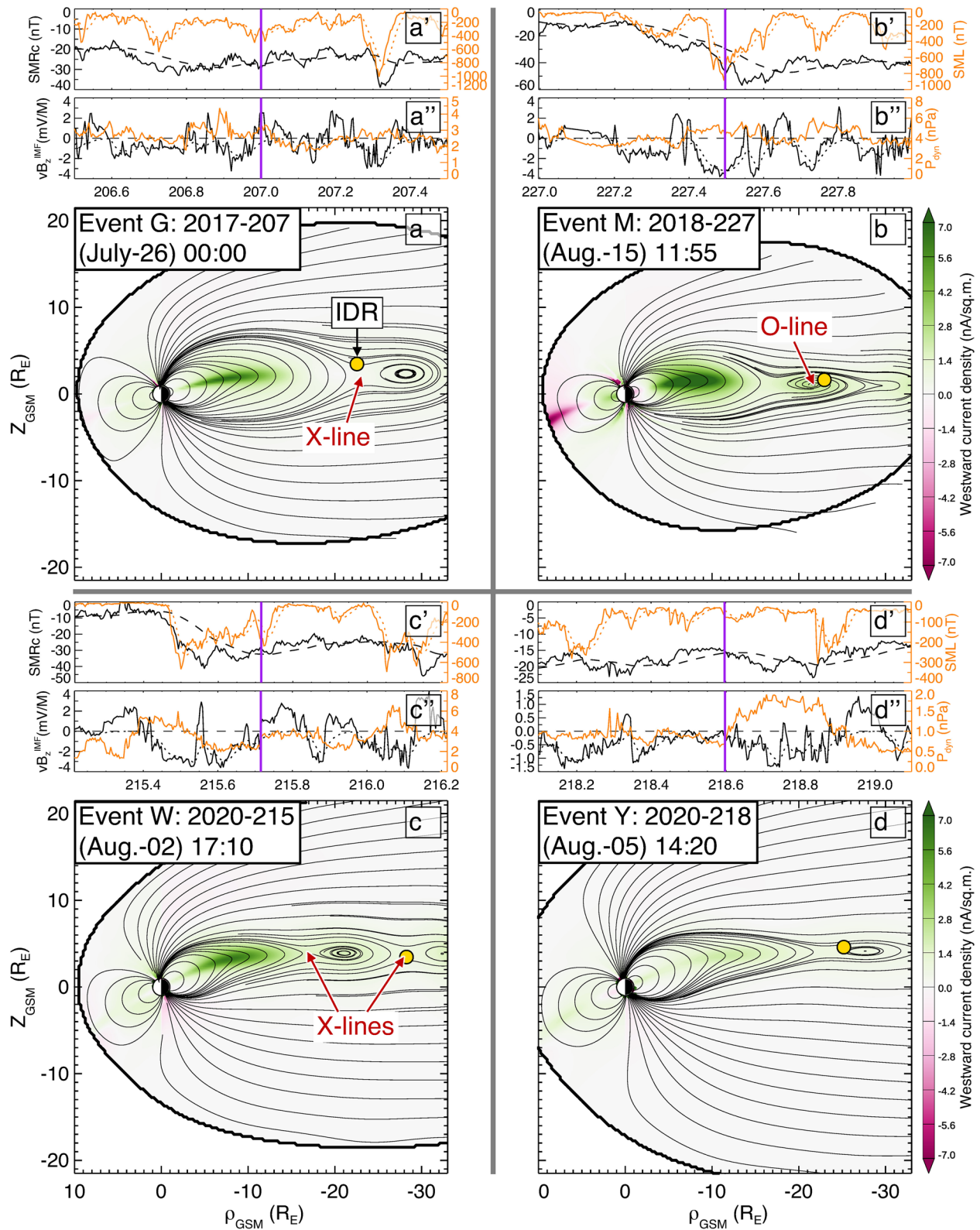


Figure 3. Ion Diffusion Regions (IDRs) against the meridional current and magnetic field distributions. (a–d) Color-coded distribution of the electric current perpendicular (westward positive) to the meridional plane, which contains the corresponding IDR (white dashed lines in Figure 2), for four events shown in Figure 2 with the similar format for global parameters (a'–d') and (a''–d'') on top of each distribution. The IDRs are shown here by large orange dots. Thin and thick lines show the magnetic field lines and the magnetospheric boundary (magnetopause).

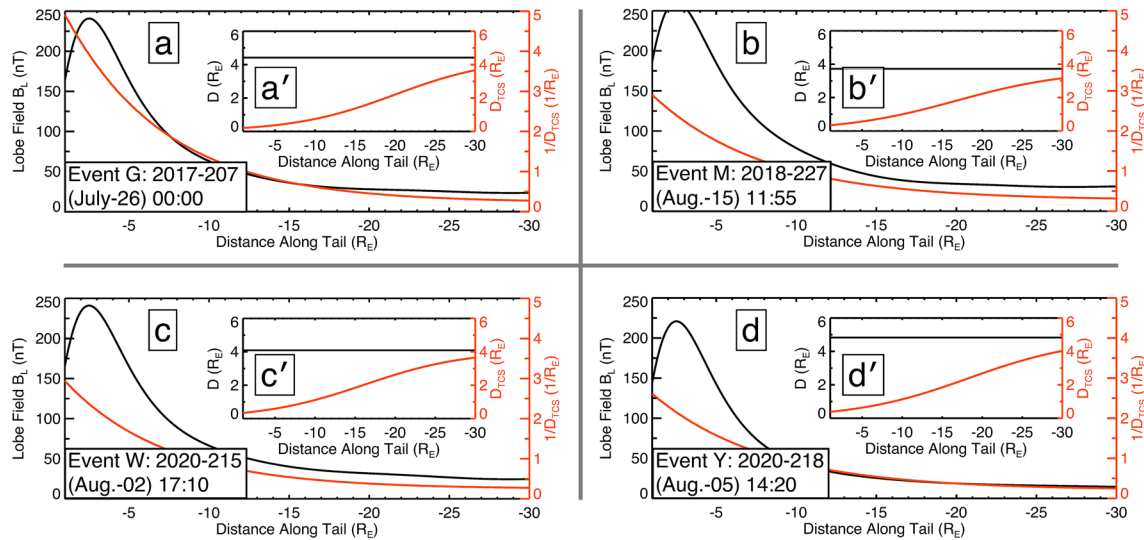


Figure 4. Profiles of the lobe field B_L and current sheet thicknesses along the tail. (a–d) 1D profiles of B_L (black line) and the inverse thin current sheet (TCS) thickness $1/D_{TCS}$ (orange line) sampled at midnight ($y = 0$) along the tail for four IDR events, G, M, W, and Y. B_L is evaluated at a height of $z = 5R_E$ above the center of the current sheet. The inset panels (a'–d') show the value 1D profiles of the current sheet thickness for the thick sheet (black constant line) and D_{TCS} (orange line).

thickening TCS at further distances down the tail. This is further illustrated in Figure 4, where the reciprocal of the TCS half-thickness, $1/D_{TCS}$, (orange lines in the main part of each panel) is compared here with the tail lobe field B_L evaluated at $z = 5R_E$ (black lines) for the main group of IDR events (G, M, W, Y). The similarity of orange and black lines throughout the tail region $-30R_E \leq x \leq -10R_E$ suggests the scaling $D_{TCS} \propto B_L^{-1}$ is formally consistent with the properties of 2D current sheet equilibria for isotropic plasmas (e.g., Sitnov & Schindler, 2010). However, closer examination reveals that the lobe field in the isotropic plasma theory should collapse with the distance from Earth given the near-Earth TCS thickness ($D_{TCS}(\rho = 0) = 0.17 - 0.34R_E$ consistent with observations that the TCS half-thickness is comparable to the thermal ion gyroradius in the field B_L [Runov et al., 2005]) much faster compared to its profiles shown in Figure 4 and consistent with earlier statistical results (Wang et al., 2004). For instance, for 2D equilibria with the constant ratio B_z/B_L (e.g., Sitnov & Merkin, 2016; Sitnov & Schindler, 2010), the lobe field should scale as $\exp(-(x/D_{TCS}(\rho = 0))(B_z/B_L))$, and even with $B_z \sim 3$ nT and $B_L \sim 100$ nT it would collapse much faster, compared to reconstructions shown in Figure 3. Besides, the conventional 2D isotropic plasma equilibria do not explain the multiscale structure of the tail with a TCS embedded into a thicker plasma sheet.

Meanwhile, the observed scaling $D_{TCS} \propto B_L^{-1}$ with the actual (reconstructed from data) lobe magnetic field is quite consistent with the equilibrium theory of TCS provided by the Speiser orbits (Sitnov & Merkin, 2016). In particular, the x-scale of TCS $L_x \sim D_{TCS}(B_L/B_z)$ ($D/D_{TCS} \gg D_{TCS}(B_L/B_z)$). Thus, the present DM reconstruction supports modern kinetic TCS models taking the quasi-adiabatic dynamics of Speiser ions into account. The insets in Figure 4 show the half-thicknesses of the two current sheets represented by Equation 10 along the tail, with the constant value of the thicker sheet (D black line) plotted against the variable thickness of the TCS (D_{TCS} orange line), demonstrating that D_{TCS} approaches D at increasing tail distances but is constrained to be $D_{TCS} < D$. Note that we neglected the possible radial dependence of the thick current sheet thickness D , similar to Equation 11, largely to avoid overfitting. We plan to further investigate the tail current sheet structure in future studies.

3.3. Special Cases

Special considerations were taken in regards to events R and T. For event R, the initial reconstruction placed the location of the central plasma sheet $\sim 3R_E$ below the MMS spacecraft during the IDR observation. Upon further inspection, the event was found to have an anomalously large value of B_y^{MF} over the preceding 30 min, with a value of ~ 8 nT. Large magnitudes of y component of the IMF are known to significantly impact the shape of the magnetotail specifically through the twisting of the plasma sheet (Tsyganenko et al., 2015; Tsyganenko & Fairfield, 2004). Although this feature is included in the structure of the model through the warping and twisting

deformation equations, via the parameter TW (Tsyganenko, 1998), its impact is presumably not captured in the storm/substorm state-space represented by Equations 1–5. Indeed, computing TW using the empirical relationship from Tsyganenko and Fairfield (2004) (see their Equations 1 and 5), results in $TW = 1.11 \times 10^{-2}$, the largest magnitude across all 26 events and being a factor of two larger than the next highest and a factor of five higher than the average event. Thus, event R was reconstructed using this empirical value and not the value obtained during the fit ($TW = 2.64 \times 10^{-3}$). As earlier studies were primarily concerned with the inner magnetosphere and/or the near-tail region, they probably neglected to observe this inconsistency. In future studies, particularly of the mid-tail, this issue should be remedied. One potential solution is to explicitly add a dimension to the state-space that correlates to the twisting effect, for instance the value of B_y^{IMF} itself or the IMF clock angle. However, owing to the “curse of dimensionality” (Verleysen & François, 2005), expanding the state-space may dilute its sensitivity to the storm and substorm features sought. Another solution that is potentially more robust is to exclude TW from the set of free parameters that is determined when fitting to data and instead replace it with an ad-hoc functional form such as the empirical relationship from Tsyganenko and Fairfield (2004) or Tsyganenko et al. (2015).

In event T, the original reconstruction with $\sigma = 0.3$ underresolved the X-line, apparently because of the unusual IMF structure ($|B_z| \sim |B_x| \sim |B_y| \sim 6$ nT). To mitigate this issue, we slightly reduced the weighting parameter to $\sigma = 0.25$.

4. Validation and Uncertainty Quantification

Examples of in situ validation of these global reconstructions are shown in Figures 5a–5d for the MMS4 magnetic field observations of the tail during events G, M, W, and Y (only observations from MMS4 are shown as the observations from the other three spacecraft are very similar). It reveals relatively large deviations in the magnetic field components $B_{x,y}$ parallel to the current plane (Figures 5a and 5b). They are likely caused by the flapping North-South motions of the current sheet as a whole (Sergeev et al., 2006) that were found in MMS observations as well (Farrugia et al., 2021). These motions are spontaneous and may appear in different phases of activity, so it is not surprising that they are not captured by the DM reconstructions. At the same time, the B_z magnetic field is reproduced even better than it appears in observations after 5 min averages (compare the black line in Figure 4c with the inset in Figure 1). Thus, hitting 24 out of 26 IDRs, achieved in this study, shows (a) how to overcome the curse of data paucity for in situ data and (b) presents solid evidence that not only validates our DM reconstructions, but also helps understand the reconnection mechanisms and its consequences.

The fidelity of the present reconstructions can also be seen from the uncertainty analysis presented in Figures 5e–5i. It compares five original binning parameters (black lines; Equations 1–5) of the magnetosphere with their means (dark blue lines) and standard deviations (light blue envelopes) over the NN subsets. The closeness of means to the original parameters G_{1-5} and small relative values of deviations suggest that the selected NNs closely follow the magnetospheric dynamics, especially on substorm scales (Figures 5g–5h).

5. Global X-Line Structure in the Context of Substorm Activity

Since the main key to the present global X-line reconstructions has been the recurring nature of substorms and storms, it is interesting to check the evolution of X-lines within a substorm cycle. Indeed, some of the considered IDRs belong to classic substorms: C and D (14:35–17:25 UT), H (06:00–08:30 UT), M (09:35–14:55 UT), U (03:00–06:00). Here we consider in more detail the 26 July 2017 substorm containing event H. The equatorial B_z distributions in the growth, expansion, and recovery phases of this substorm are shown in Figure 6 and animated with 5 min cadence in Movie S1, with event H shown in Figure 6e. The onset of this substorm (Figure 6d) is marked by the formation of a new X-line $\approx 24R_E$ from the Earth, which fades away later in the recovery phase (Figure 6f). This evolution picture is consistent the original description of the substorm cycle (Baker et al., 1996; Hones, 1984).

Note that this is not the only X-line in this global picture, as the reconstructions also show the persistent presence of a more distant X-line beyond $\approx 24R_E$ distance (e.g., at $r \approx 28R_E$ in Figure 6e). In contrast to the widespread prejudice that magnetic reconnection only occurs with the onset of a substorm, the existence of such a pre-onset X-line was conjectured already in the seminal paper by Hones (1984). Moreover, without the formation of such an X-line and a relatively steady reconnection there it is difficult to explain observations of the lobe magnetic flux saturation in the last 40 min for a significant fraction of substorm growth phases (Shukhtina et al., 2014). Two X-lines with relatively steady (around $30R_E$) and unsteady (around $20R_E$) reconnection regimes were resolved

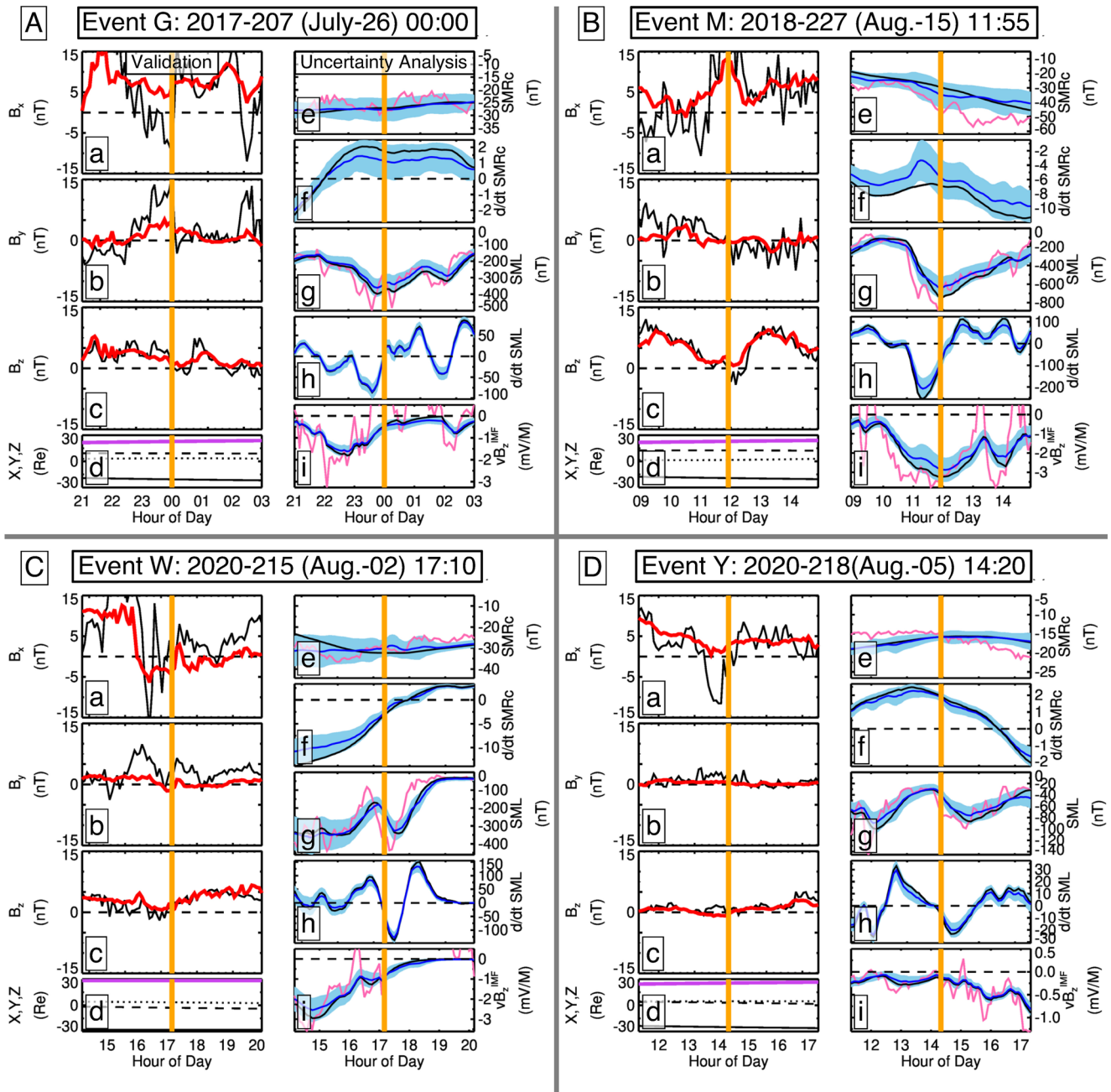


Figure 5. Validation and uncertainty analysis for events G, M, W, and Y, labeled (A–D) respectively. (a–c) The observed MMS4 5 min averaged GSM magnetic field components (black lines) and their DM reconstructions (red lines). (d) MMS ephemeris (in GSM) X (solid line), Y (dashed line), Z (dash-dotted line), and the radial distance (pink line). (e–i) The storm/substorm state binning parameters $\langle \text{SMRc} \rangle$, $\langle D(\text{SMRc}/Dt) \rangle$, $\langle \text{SML} \rangle$, $\langle D(\text{SML}/Dt) \rangle$, and $\langle vB_z^{IMF} \rangle$ as described in Section 2.2, shown by black lines as compared to their means over the nearest neighbors (NNs; blue lines). The light blue shading shows the standard deviations $\pm 1\sigma$ of the NNs. Pink lines in (e, g, and i) show the original 5 min OMNI data for the parameters SMRc (pressure-corrected SMR [Tsyganenko et al., 2021]), SML, and vB_z^{IMF} . Yellow vertical lines indicate the moment of the spatial reconstructions shown in the previous figures.

using the DM approach by Sitnov et al. (2021) who explicitly evaluated the steadiness of reconnection by investigating the meridional distributions of the in-plane (B_x and B_z) components of the magnetic field before and after onset and invoking the Faraday's law $\partial E_y/\partial x = -\partial B_z/\partial t$, $\partial E_x/\partial z = \partial B_y/\partial t$. They also compared the results with 3D PIC simulations of the tail equilibria that revealed similar X-lines with steady and unsteady reconnection.

The general misconception that the change of magnetic topology always results in explosive reconnection is at variance with the large family of self-consistent X-line plasma equilibria (e.g., Yoon & Lui, 2005, and refs.

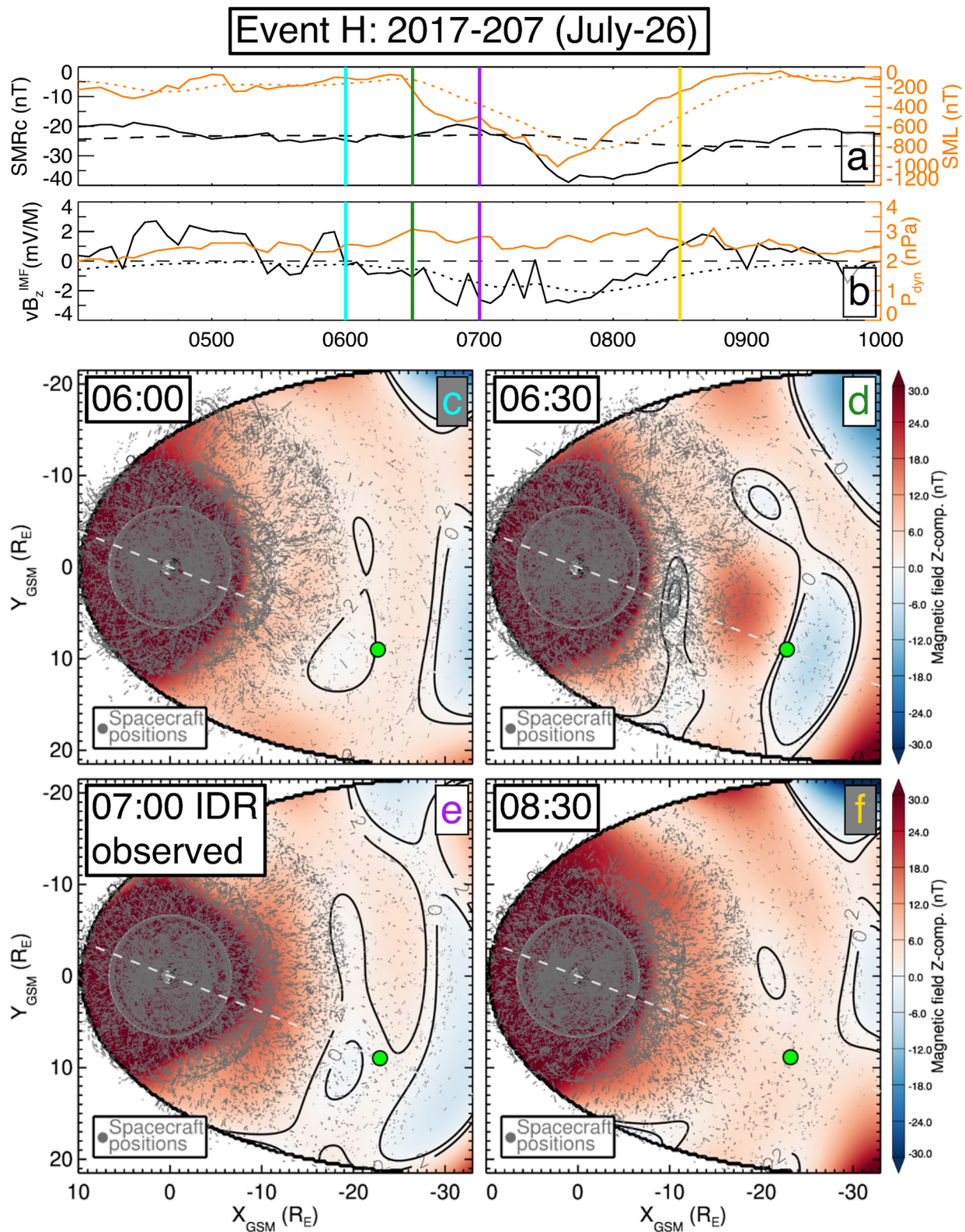


Figure 6. Evolution of X-lines during the 26 July 2017 substorm containing event H (panel (e)). (a and b) Geomagnetic indices and solar wind parameters in a format as shown previously. (c–f) Equatorial magnetic field, B_z , snapshots in a similar format as Figure 2 for four different times during the 26 July 2017 substorm. The four times are indicated in panels (a and b) by the vertical lines.

therein). Their PIC simulations reveal both active reconnection regimes (Sitnov & Swisdak, 2011) and steady configurations (Sitnov et al., 2013). After all, stagnant plasmoids are known in observations (e.g., Nishida et al., 1986). It is also worth noting here that the statistics of bursty bulk flows (Juusola et al., 2011) suggests that X-lines (and the corresponding fast flows) can appear in any phases of substorms.

Other substorms associated with events C/D, M, and U show similar “classic substorm” signatures with the new X-lines arising at the onset and fading away at the end of the recovery phase. In cases of weaker substorms (events C and D with $\min(\text{SML}) > -400$ nT), the new X-lines are less pronounced (Figures S2 in Supporting Information S1). In case of storm-time substorms (event M), the B_z variations, and especially dipolarization effects are much stronger (Figure 2b). At the same time, new X-lines may form closer to the Earth ($\sim 15R_E$) consistent with in situ observations (Angelopoulos et al., 2020).

As an example of relatively unusual substorm activity associated with the reconstructed X-lines we consider the tail evolution around event Y that occurred on 5 August 2020 at 14:20 UT. According to Figure 7e (red line), during this event, the reconstructed B_z component becomes negative at 13:15 UT and continues to be negative through 14:20 UT. Event Y corresponds to a marked reduction of the SML index (Figure 5). Therefore, at first sight, magnetic reconnection starts well before the substorm onset, even before the beginning of the growth phase of this substorm. This inconsistency (the gap between the red and black lines in Figure 7e) appears to be confirmed by MMS4 observations, which show positive B_z during the interval 13:35–14:10 UT (black line) in contrast to a negative B_z in the DM reconstructions (red line). MMS observations also suggest that the plasma sheet was quiet during that period (Figure 7a).

However, closer examination shows a more complex picture with far better consistency between the DM reconstructions, ground-based data, and in situ observations. First, according to Figure 5, the reconstructed B_z becomes negative in the midst of the recovery phase of an earlier substorm ($\sim 13:00$ UT), with a persistent solar wind input $vB_z < 0$ for about 2 hr prior to event Y (Figure 5).

Second, according to Figures 7b–7e, during the last 30 min before event Y (13:40–14:10 UT) MMS was outside the plasma sheet with $|B_x| \sim 10$ nT and a plasma β generally less than unity. Moreover, the positive B_z profile correlated with B_x and B_y enhancements suggesting that the current sheet was bent or flapping and that the observed positive B_z was a consequence. In any case, the measured positive B_z was not observed while MMS was in the plasma sheet. Furthermore, during the earlier period (13:15–13:30 UT), when MMS was indeed inside the plasma sheet, it did observe significant tailward plasma flows, consistent with our reconstruction of another $B_z = 0$ crossing (O-line) around 13:15 UT (Figure 7a). In other words, prior to event Y, the plasma sheet was active and its activity matched our reconstructed magnetic field. Before 13:00 there was no inconsistency between our reconstructions and MMS observations at all (the error is less than 1 nT). Thus, our magnetic field reconstruction is quite consistent with MMS data, both the magnetic field and plasma data.

6. Conclusions

The consistency of the DM picture of the 2017–2020 MMS IDR alphabet suggests that, in spite of the extreme paucity of in situ observations, DM successfully reconstructs the overall structure of magnetotail X- and O-lines implying they are strongly self-organized on the global scale. It also supports Speiser proton orbits as the theoretical mechanism for the formation of an embedded TCS in the magnetotail. The X-lines vary in length from 5 to $40R_E$, with the shorter ones tending to form inside of $\sim 20R_E$ while the longer ones, $\sim 40R_E$, appear beyond $25R_E$. The concurrent appearance of such near-Earth and midtail X-lines is consistent with the original conjectures regarding new X-line formation during substorms (Hones, 1984). It also explains the detection of X-lines as discrete points in radial distance in remote sensing (Angelopoulos et al., 2013; Figure 3c) as well as the stepwise retreat of magnetic reconnection regions suggested by their auroral manifestations and confirmed by in situ observations (Ieda et al., 2016). The persistent formation of X-lines near $30R_E$ has also been confirmed by the statistical analysis of the traveling compression regions (Imber et al., 2011). The success of our X-line reconstruction indicates that year after year, the spatial/temporal patterns of storms and substorms in the Earth's magnetotail are highly recurrent and hence reproducible with historic data, while magnetic reconnection controls the global state of the magnetosphere reflected in its activity indices, their trends, and the solar wind energy input.

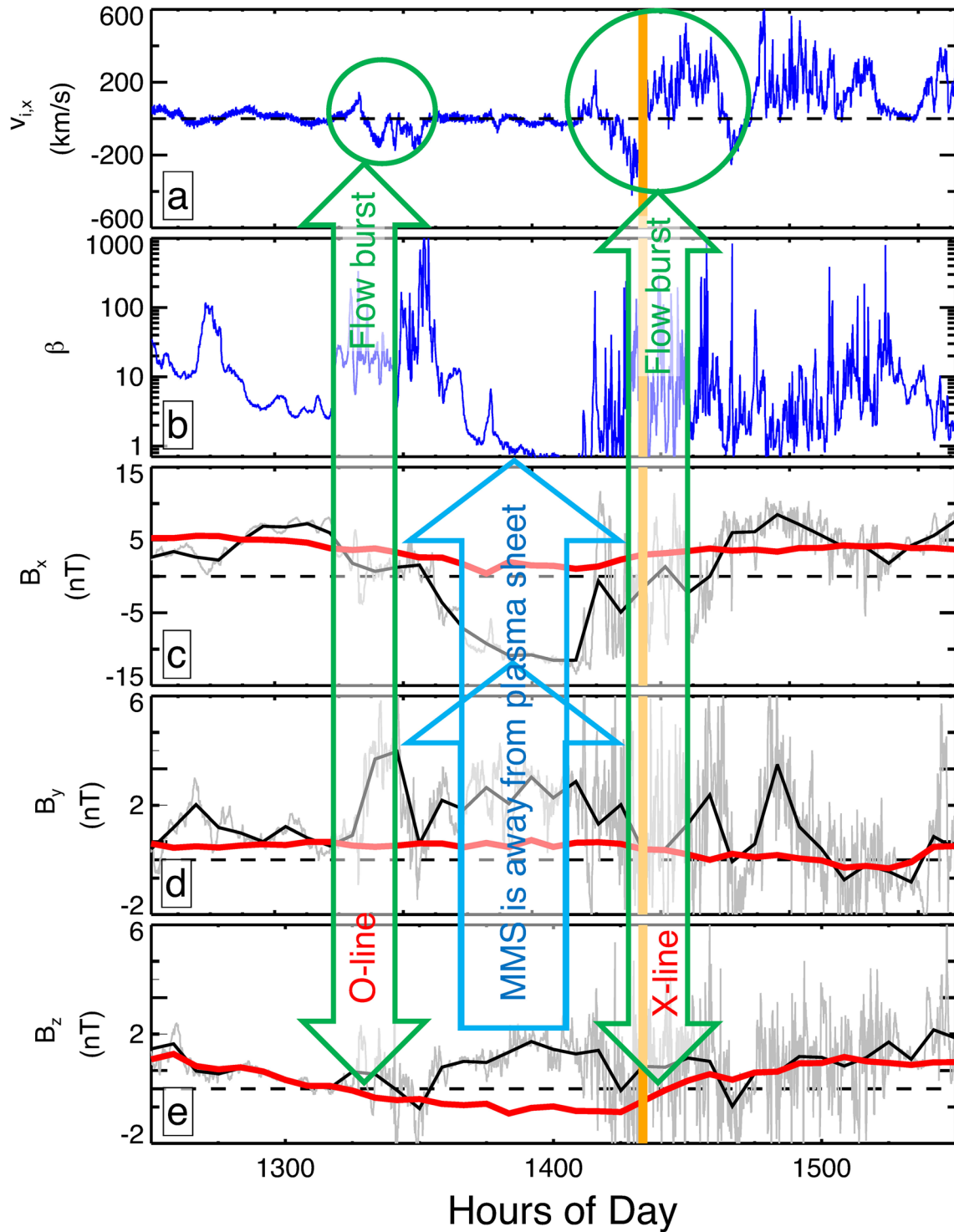


Figure 7. Unusual substorm activity around event Y. (a) The ion bulk flow velocity, $v_{i,x}$. (b) Plasma beta computed from measurements of ions. (c–e) The observed MMS4 5 min averaged GSM magnetic field components (black lines) and their DM reconstructions (red lines) similar to Figures 5 but with different ranges. Light gray lines show the magnetic field components before the averaging.

Data Availability Statement

The data used in the paper are archived on Zenodo (Stephens et al., 2022). For each of the 26 IDR events, files are included that detail: time intervals identified using the nearest-neighbor search and the resulting subset of

magnetometer data and their associated weights, files containing the fit set of coefficients and parameters for the model, and the digital model output data that were used in constructing the figures. The compiled magnetometer database used in this study is available on the SPDF website (Korth et al., 2018). This study extended this database with the addition of MMS magnetometer data which has also been included in the Zenodo archive. The SMR and SML indices obtained from the SuperMAG web page are also included in the Zenodo archive. The data describing the solar wind conditions were taken from the 5 min OMNI data (Papitashvili & King, 2020).

Acknowledgments

The authors acknowledge useful discussions with G. Clark, R. Nakamura, S. Sharma, H. Spence, V. Titov, J. Vandegriff, D. Vassiliadis, and J. Zhang. They thank the SuperMag team and their collaborators, which provided the global indices of the storm and substorm activity. They also thank the teams who created and provided Geotail, Polar, IMP 8, Cluster, THEMIS, Van Allen Probes, MMS and GOES data obtained via NSSDC CDAWeb online facility, as well as Wind and ACE solar wind/IMF data that went into the production of the OMNI data obtained via NASA/GSFC's Space Physics Data Facility's OMNI-Web service. This work was funded by NASA Grants 80NSSC19K0074, 80NSSC20K1271, 80NSSC20K1787, as well as NSF Grants AGS-1702147 and AGS-1744269. N. A. Tsyganenko acknowledges support of the RFBR Grant 20-05-00218. The work on this paper for MIS and GKS also benefited greatly from the discussions at the ISSI workshops, "Magnetotail Dipolarizations: Archimedes Force or Ideal Collapse?" and "Imaging the invisible: Unveiling the global structure of Earth's dynamic magnetosphere", held in May 2022.

References

- Alken, P., Thébault, E., Beggan, C. D., Amit, H., Aubert, J., Baerenzung, J., & Zhou, B. (2021). International geomagnetic reference field: The thirteenth generation. *Earth, Planets, and Space*, 73(1), 49. <https://doi.org/10.1186/s40623-020-01288-x>
- Angelopoulos, V., Artemyev, A., Phan, T. D., & Miyashita, Y. (2020). Near-Earth magnetotail reconnection powers space storms. *Nature Physics*, 16(3), 317–321. <https://doi.org/10.1038/s41567-019-0749-4>
- Angelopoulos, V., McFadden, J. P., Larson, D., Carlson, C. W., Mende, S. B., Frey, H., & Kepko, L. (2008). Tail reconnection triggering substorm onset. *Science*, 321(5891), 931–935. <https://doi.org/10.1126/science.1160495>
- Angelopoulos, V., Runov, A., Zhou, X.-Z., Turner, D. L., Kiehas, S. A., Li, S.-S., & Shinohara, I. (2013). Electromagnetic energy conversion at reconnection fronts. *Science*, 341(6153), 1478–1482. <https://doi.org/10.1126/science.1236992>
- Baker, D. N., Pulkkinen, T. I., Angelopoulos, V., Baumjohann, W., & McPherron, R. L. (1996). Neutral line model of substorms: Past results and present view. *Journal of Geophysical Research: Space Physics*, 101(A6), 12975–13010. <https://doi.org/10.1029/95JA03753>
- Birn, J., Hesse, M., & Schindler, K. (1996). MHD simulations of magnetotail dynamics. *Journal of Geophysical Research: Space Physics*, 101(A6), 12939–12954. <https://doi.org/10.1029/96JA00611>
- Borovsky, J. E., & Yakymenko, K. (2017). Substorm occurrence rates, substorm recurrence times, and solar wind structure. *Journal of Geophysical Research: Space Physics*, 122(3), 2973–2998. <https://doi.org/10.1002/2016JA023625>
- Burch, J. L., Moore, T. E., Torbert, R. B., & Giles, B. L. (2016). Magnetospheric multiscale overview and science objectives. *Space Science Reviews*, 199(1–4), 5–21. <https://doi.org/10.1007/s11214-015-0164-9>
- Burch, J. L., Torbert, R. B., Phan, T. D., Chen, L.-J., Moore, T. E., Ergun, R. E., & Chandler, M. (2016). Electron-scale measurements of magnetic reconnection in space. *Science*, 352(6290). <https://doi.org/10.1126/science.aaf2939>
- Burton, R. K., McPherron, R. L., & Russell, C. T. (1975). An empirical relationship between interplanetary conditions and *Dst*. *Journal of Geophysical Research*, 80(31), 4204–4214. <https://doi.org/10.1029/JA080i031p04204>
- Camporeale, E. (2019). The challenge of machine learning in space weather: Nowcasting and forecasting. *Space Weather*, 17(8), 1166–1207. <https://doi.org/10.1029/2018SW002061>
- Chen, L.-J., Wang, S., Hesse, M., Ergun, R. E., Moore, T., Giles, B., & Lindqvist, P.-A. (2019). Electron diffusion regions in magnetotail reconnection under varying guide fields. *Geophysical Research Letters*, 46(12), 6230–6238. <https://doi.org/10.1029/2019GL082393>
- Childs, H., Brugger, E., Whitlock, B., Meredith, J., Ahern, S., Pugmire, D., & Navrátil, P. (2012). Visit: An end-user tool for visualizing and analyzing very large data. In *High performance visualization-enabling extreme-scale scientific insight* (pp. 357–372). <https://doi.org/10.1201/b12985>
- Cowley, S. (1981). Magnetospheric asymmetries associated with the y-component of the IMF. *Planetary and Space Science*, 29(1), 79–96. [https://doi.org/10.1016/0032-0633\(81\)90141-0](https://doi.org/10.1016/0032-0633(81)90141-0)
- Dungey, J. W. (1961). Interplanetary magnetic field and the auroral zones. *Physical Review Letters*, 6, 47–48. <https://doi.org/10.1103/PhysRevLett.6.47>
- Eastwood, J. P., Phan, T. D., Øieroset, M., & Shay, M. A. (2010). Average properties of the magnetic reconnection ion diffusion region in the earth's magnetotail: The 2001–2005 Cluster observations and comparison with simulations. *Journal of Geophysical Research: Space Physics*, 115(A8). <https://doi.org/10.1029/2009JA014962>
- Farrugia, C. J., Rogers, A. J., Torbert, R. B., Genestreti, K. J., Nakamura, T. K. M., Lavraud, B., & Dors, I. (2021). An encounter with the ion and electron diffusion regions at a flapping and twisted tail current sheet. *Journal of Geophysical Research: Space Physics*, 126(3), e2020JA028903. <https://doi.org/10.1029/2020JA028903>
- Fuselier, S. A., Trattner, K. J., & Petrinec, S. M. (2011). Antiparallel and component reconnection at the dayside magnetopause. *Journal of Geophysical Research: Space Physics*, 116(A10). <https://doi.org/10.1029/2011JA016888>
- Gjerloev, J. W. (2012). The SuperMag data processing technique. *Journal of Geophysical Research: Space Physics*, 117(A9). <https://doi.org/10.1029/2012JA017683>
- Gonzalez, W. D., Joselyn, J. A., Kamide, Y., Kroehl, H. W., Rostoker, G., Tsurutani, B. T., & Vasyliunas, V. M. (1994). What is a geomagnetic storm? *Journal of Geophysical Research: Space Physics*, 99(A4), 5771–5792. <https://doi.org/10.1029/93JA02867>
- Greene, J. M. (1988). Geometrical properties of three-dimensional reconnecting magnetic fields with nulls. *Journal of Geophysical Research: Space Physics*, 93(A8), 8583–8590. <https://doi.org/10.1029/JA093iA08p08583>
- Griton, L., Pantellini, F., & Meliani, Z. (2018). Three-dimensional magnetohydrodynamic simulations of the solar wind interaction with a hyperfast-rotating Uranus. *Journal of Geophysical Research: Space Physics*, 123(7), 5394–5406. <https://doi.org/10.1029/2018JA025331>
- Hones, E. W., Jr. (1984). Plasma sheet behavior during substorms. In *Magnetic reconnection in space and laboratory plasmas* (pp. 178–184). American Geophysical Union (AGU). <https://doi.org/10.1029/GM030p0178>
- Ieda, A., Nishimura, Y., Miyashita, Y., Angelopoulos, V., Runov, A., Nagai, T., & Machida, S. (2016). Stepwise tailward retreat of magnetic reconnection: THEMIS observations of an auroral substorm. *Journal of Geophysical Research: Space Physics*, 121(5), 4548–4568. <https://doi.org/10.1002/2015JA022244>
- Imber, S. M., Slavin, J. A., Auster, H. U., & Angelopoulos, V. (2011). A THEMIS survey of flux ropes and traveling compression regions: Location of the near-earth reconnection site during solar minimum. *Journal of Geophysical Research: Space Physics*, 116(A2). <https://doi.org/10.1029/2010JA016026>
- Jackson, D. D. (1972). Interpretation of inaccurate, insufficient and inconsistent data. *Geophysical Journal International*, 28(2), 97–109. <https://doi.org/10.1111/j.1365-246X.1972.tb06115.x>
- Ji, H., Daughton, W., Jara-Almonte, J., Le, A., Stanier, A., & Yoo, J. (2022). Magnetic reconnection in the era of exascale computing and multi-scale experiments. *Nature Reviews Physics*, 4, 263–282. <https://doi.org/10.1038/s42254-021-00419-x>

- Juusola, L., Østgaard, N., Tanskanen, E., Partamies, N., & Snekvik, K. (2011). Earthward plasma sheet flows during substorm phases. *Journal of Geophysical Research: Space Physics*, *116*(A10). <https://doi.org/10.1029/2011JA016852>
- Korth, H., Sitnov, M. I., & Stephens, G. K. (2018). Magnetic field modeling database description final [Dataset]. NASA Space Physics Data Facility. Retrieved from https://spdf.gsfc.nasa.gov/pub/data/aaa_special-purpose-datasets/empirical-magnetic-field-modeling-database-with-TS07D-coefficients/
- Liemohn, M. W., McCollough, J. P., Jordanova, V. K., Ngwira, C. M., Morley, S. K., Cid, C., & Vasile, R. (2018). Model evaluation guidelines for geomagnetic index predictions. *Space Weather*, *16*(12), 2079–2102. <https://doi.org/10.1029/2018SW002067>
- Liu, R., Kliem, B., Titov, V. S., Chen, J., Wang, Y., Wang, H., et al. (2016). Structure, stability, and evolution of magnetic flux ropes from the perspective of magnetic twist. *The Astrophysical Journal*, *818*(2), 148. <https://doi.org/10.3847/0004-637x/818/2/148>
- McPherron, R. L., Russell, C. T., & Aubry, M. P. (1973). Satellite studies of magnetospheric substorms on 15 August 1968: 9. Phenomenological model for substorms. *Journal of Geophysical Research*, *78*(16), 3131–3149.
- Mead, G. D., & Beard, D. B. (1964). Shape of the geomagnetic field solar wind boundary. *Journal of Geophysical Research*, *69*(7), 1169–1179. <https://doi.org/10.1029/JZ069i007p01169>
- Nagai, T., Fujimoto, M., Nakamura, R., Baumjohann, W., Ieda, A., Shinohara, I., & Mukai, T. (2005). Solar wind control of the radial distance of the magnetic reconnection site in the magnetotail. *Journal of Geophysical Research: Space Physics*, *110*(A9). <https://doi.org/10.1029/2005JA011207>
- Nagai, T., & Shinohara, I. (2022). Solar wind energy input: The primary control factor of magnetotail reconnection site. *Journal of Geophysical Research: Space Physics*, *127*(8). e2022JA030653. <https://doi.org/10.1029/2022JA030653>
- Nelder, J. A., & Mead, R. (1965). A simplex method for function minimization. *The Computer Journal*, *7*(4), 308–313. <https://doi.org/10.1093/comjnl/7.4.308>
- Newell, P. T., & Gjerloev, J. W. (2011). Evaluation of SuperMag auroral electrojet indices as indicators of substorms and auroral power. *Journal of Geophysical Research: Space Physics*, *116*(A12). <https://doi.org/10.1029/2011JA016779>
- Newell, P. T., & Gjerloev, J. W. (2012). SuperMag-based partial ring current indices. *Journal of Geophysical Research: Space Physics*, *117*(A5). <https://doi.org/10.1029/2012JA017586>
- Nishida, A., Scholer, M., Terasawa, T., Bame, S. J., Gloeckler, G., Smith, E. J., & Zwickl, R. D. (1986). Quasi-stagnant plasmoid in the middle tail: A new pre-expansion phase phenomenon. *Journal of Geophysical Research: Space Physics*, *91*(A4), 4245–4255. <https://doi.org/10.1029/JA091iA04p04245>
- Papitashvili, N. E., & King, J. H. (2020). OMNI 5 min data [Dataset]. NASA Space Physics Data Facility. Retrieved from <https://www.unavco.org/data/doi/10.7283/633E-1497>
- Partamies, N., Juusola, L., Tanskanen, E., & Kauristie, K. (2013). Statistical properties of substorms during different storm and solar cycle phases. *Annales Geophysicae*, *31*(2), 349–358. <https://doi.org/10.5194/angeo-31-349-2013>
- Phan, T. D., Eastwood, J. P., Shay, M. A., Drake, J. F., Sonnerup, B. U. Ö., Fujimoto, M., & Magnes, W. (2018). Electron magnetic reconnection without ion coupling in Earth's turbulent magnetosheath. *Nature*, *557*(7704), 202–206. <https://doi.org/10.1038/s41586-018-0091-5>
- Press, W. H., Teukolsky, S. A., Flannery, B. P., & Vetterling, W. T. (1992). *Numerical recipes in FORTRAN: The art of scientific computing* (2nd ed.). Cambridge University Press.
- Reyes, P. I., Pinto, V. A., & Moya, P. S. (2021). Geomagnetic storm occurrence and their relation with solar cycle phases. *Space Weather*, *19*(9), e2021SW002766. <https://doi.org/10.1029/2021SW002766>
- Rogers, A. J., Farrugia, C. J., & Torbert, R. B. (2019). Numerical algorithm for detecting ion diffusion regions in the geomagnetic tail with applications to MMS tail season 1 May to 30 September 2017. *Journal of Geophysical Research: Space Physics*, *124*(8), 6487–6503. <https://doi.org/10.1029/2018JA026429>
- Rogers, A. J., Farrugia, C. J., Torbert, R. B., & Rogers, T. J. (2023). Applying magnetic curvature to MMS data to identify thin current sheets relative to tail reconnection. *Journal of Geophysical Research: Space Physics*, *128*, e2022JA030577. <https://doi.org/10.1029/2022JA030577>
- Runov, A., Sergeev, V. A., Baumjohann, W., Nakamura, R., Apatenkov, S., Asano, Y., & Rème, H. (2005). Electric current and magnetic field geometry in flapping magnetotail current sheets. *Annales Geophysicae*, *23*(4), 1391–1403. <https://doi.org/10.5194/angeo-23-1391-2005>
- Russell, C. T., & McPherron, R. L. (1973). The magnetotail and substorms. *Space Science Reviews*, *15*(2), 205–266. <https://doi.org/10.1007/BF00169321>
- Sergeev, V. A., Angelopoulos, V., Kubyskhina, M., Donovan, E., Zhou, X.-Z., Runov, A., & Nakamura, R. (2011). Substorm growth and expansion onset as observed with ideal ground-spacecraft THEMIS coverage. *Journal of Geophysical Research: Space Physics*, *116*(A5). <https://doi.org/10.1029/2010JA015689>
- Sergeev, V. A., Sormakov, D. A., Apatenkov, S. V., Baumjohann, W., Nakamura, R., Runov, A. V., & Nagai, T. (2006). Survey of large-amplitude flapping motions in the midtail current sheet. *Annales Geophysicae*, *24*(7), 2015–2024. <https://doi.org/10.5194/angeo-24-2015-2006>
- Shiota, D., Isobe, H., Chen, P. F., Yamamoto, T. T., Sakajiri, T., & Shibata, K. (2005). Self-consistent magnetohydrodynamic modeling of a coronal mass ejection, coronal dimming, and a giant cusp-shaped arcade formation. *The Astrophysical Journal*, *634*(1), 663–678. <https://doi.org/10.1086/496943>
- Shue, J.-H., Song, P., Russell, C. T., Steinberg, J. T., Chao, J. K., Zastenker, G., & Kawano, H. (1998). Magnetopause location under extreme solar wind conditions. *Journal of Geophysical Research: Space Physics*, *103*(A8), 17691–17700. <https://doi.org/10.1029/98JA01103>
- Shukhtina, M. A., Dmitrieva, N. P., & Sergeev, V. A. (2014). On the conditions preceding sudden magnetotail magnetic flux unloading. *Geophysical Research Letters*, *41*(4), 1093–1099. <https://doi.org/10.1002/2014GL059290>
- Sibeck, D. G., Lopez, R. E., & Roelof, E. C. (1991). Solar wind control of the magnetopause shape, location, and motion. *Journal of Geophysical Research: Space Physics*, *96*(A4), 5489–5495. <https://doi.org/10.1029/90JA02464>
- Sitnov, M. I., Birn, J., Ferdousi, B., Gordeev, E., Khotyaintsev, Y., Merkin, V., & Zhou, X. (2019). Explosive magnetotail activity. *Space Science Reviews*, *215*(4), 31. <https://doi.org/10.1007/s11214-019-0599-5>
- Sitnov, M. I., Buzulukova, N., Swisdak, M., Merkin, V. G., & Moore, T. E. (2013). Spontaneous formation of dipolarization fronts and reconnection onset in the magnetotail. *Geophysical Research Letters*, *40*(1), 22–27. <https://doi.org/10.1029/2012GL054701>
- Sitnov, M. I., & Merkin, V. G. (2016). Generalized magnetotail equilibria: Effects of the dipole field, thin current sheets, and magnetic flux accumulation. *Journal of Geophysical Research: Space Physics*, *121*(8), 7664–7683. <https://doi.org/10.1002/2016JA023001>
- Sitnov, M. I., & Schindler, K. (2010). Tearing stability of a multiscale magnetotail current sheet. *Geophysical Research Letters*, *37*(8). <https://doi.org/10.1029/2010GL042961>
- Sitnov, M. I., Sharma, A. S., Papadopoulos, K., & Vassiliadis, D. (2001). Modeling substorm dynamics of the magnetosphere: From self-organization and self-organized criticality to nonequilibrium phase transitions. *Physical Review E—Statistical Physics, Plasmas, Fluids, and Related Interdisciplinary Topics*, *65*, 016116. <https://doi.org/10.1103/PhysRevE.65.016116>

- Sitnov, M. I., Stephens, G. K., Motoba, T., & Swisdak, M. (2021). Data mining reconstruction of magnetotail reconnection and implications for its first-principle modeling. *Frontiers in Physics*, 9. <https://doi.org/10.3389/fphy.2021.644884>
- Sitnov, M. I., Stephens, G. K., Tsyganenko, N. A., Miyashita, Y., Merkin, V. G., Motoba, T., & Genestreti, K. J. (2019b). Signatures of nonideal plasma evolution during substorms obtained by mining multission magnetometer data. *Journal of Geophysical Research: Space Physics*, 124(11), 8427–8456. <https://doi.org/10.1029/2019JA027037>
- Sitnov, M. I., Stephens, G. K., Tsyganenko, N. A., Ukhorskiy, A. Y., Wing, S., Korth, H., & Anderson, B. J. (2017). Spatial structure and asymmetries of magnetospheric currents inferred from high-resolution empirical geomagnetic field models. In *Dawn-dusk asymmetries in planetary plasma environments* (pp. 199–212). American Geophysical Union (AGU). <https://doi.org/10.1002/9781119216346.ch15>
- Sitnov, M. I., & Swisdak, M. (2011). Onset of collisionless magnetic reconnection in two-dimensional current sheets and formation of dipolarization fronts. *Journal of Geophysical Research: Space Physics*, 116(A12). <https://doi.org/10.1029/2011JA016920>
- Sitnov, M. I., Swisdak, M., Guzdar, P. N., & Runov, A. (2006). Structure and dynamics of a new class of thin current sheets. *Journal of Geophysical Research: Space Physics*, 111(A8). <https://doi.org/10.1029/2005JA011517>
- Sitnov, M. I., Tsyganenko, N. A., Ukhorskiy, A. Y., & Brandt, P. C. (2008). Dynamical data-based modeling of the storm-time geomagnetic field with enhanced spatial resolution. *Journal of Geophysical Research: Space Physics*, 113(A7). <https://doi.org/10.1029/2007JA013003>
- Sitnov, M. I., Ukhorskiy, A. Y., & Stephens, G. K. (2012). Forecasting of global data-binning parameters for high-resolution empirical geomagnetic field models. *Space Weather*, 10(9). <https://doi.org/10.1029/2012SW000783>
- Speiser, T. W. (1965). Particle trajectories in model current sheets: 1. Analytical solutions. *Journal of Geophysical Research*, 70(17), 4219–4226. <https://doi.org/10.1029/JZ070i017p04219>
- Stephens, G. K., Bingham, S. T., Sitnov, M. I., Gkioulidou, M., Merkin, V. G., Korth, H., & Ukhorskiy, A. Y. (2020). Storm time plasma pressure inferred from multission measurements and its validation using van Allen probes particle data. *Space Weather*, 18(12), e2020SW002583. <https://doi.org/10.1029/2020SW002583>
- Stephens, G. K., & Sitnov, M. I. (2021). Concurrent empirical magnetic reconstruction of storm and substorm spatial scales using data mining and virtual spacecraft. *Frontiers in Physics*, 9, 210. <https://doi.org/10.3389/fphy.2021.653111>
- Stephens, G. K., Sitnov, M. I., Korth, H., Tsyganenko, N. A., Ohtani, S., Gkioulidou, M., & Ukhorskiy, A. Y. (2019). Global empirical picture of magnetospheric substorms inferred from multission magnetometer data. *Journal of Geophysical Research: Space Physics*, 124(2), 1085–1110. <https://doi.org/10.1029/2018JA025843>
- Stephens, G. K., Sitnov, M. I., Weigel, R., Turner, D., Tsyganenko, N., Rogers, A., et al. (2022). Global structure of magnetotail reconnection revealed by mining space magnetometer data [Dataset]. Zenodo. <https://doi.org/10.5281/zenodo.6862829>
- Tanaka, T., Ebihara, Y., Watanabe, M., Den, M., Fujita, S., Kikuchi, T., & Kataoka, R. (2021). Roles of the M-I coupling and plasma sheet dissipation on the growth-phase thinning and subsequent transition to the onset. *Journal of Geophysical Research: Space Physics*, 126(12), e2021JA029925. <https://doi.org/10.1029/2021JA029925>
- Torbert, R. B., Burch, J. L., Phan, T. D., Hesse, M., Argall, M. R., Shuster, J., & Saito, Y. (2018). Electron-scale dynamics of the diffusion region during symmetric magnetic reconnection in space. *Science*, 362(6421), 1391–1395. <https://doi.org/10.1126/science.aat2998>
- Tsyganenko, N. A. (1991). Methods for quantitative modeling of the magnetic field from Birkeland currents. *Planetary and Space Science*, 39(4), 641–654. [https://doi.org/10.1016/0032-0633\(91\)90058-I](https://doi.org/10.1016/0032-0633(91)90058-I)
- Tsyganenko, N. A. (1995). Modeling the Earth's magnetospheric magnetic field confined within a realistic magnetopause. *Journal of Geophysical Research: Space Physics*, 100(A4), 5599–5612. <https://doi.org/10.1029/94JA03193>
- Tsyganenko, N. A. (1998). Modeling of twisted/warped magnetospheric configurations using the general deformation method. *Journal of Geophysical Research: Space Physics*, 103(A10), 23551–23563. <https://doi.org/10.1029/98JA02292>
- Tsyganenko, N. A. (2002a). A model of the near magnetosphere with a dawn-dusk asymmetry 1. Mathematical structure. *Journal of Geophysical Research: Space Physics*, 107(A8), SMP12-1–SMP12-15. <https://doi.org/10.1029/2001JA000219>
- Tsyganenko, N. A. (2002b). A model of the near magnetosphere with a dawn-dusk asymmetry 2. Parameterization and fitting to observations. *Journal of Geophysical Research: Space Physics*, 107(A8), SMP10-1–SMP10-17. <https://doi.org/10.1029/2001JA000220>
- Tsyganenko, N. A. (2013). Data-based modeling of the Earth's dynamic magnetosphere: A review. *Annales Geophysicae*, 31(10), 1745–1772. <https://doi.org/10.5194/angeo-31-1745-2013>
- Tsyganenko, N. A. (2014). Data-based modeling of the geomagnetosphere with an IMF-dependent magnetopause. *Journal of Geophysical Research: Space Physics*, 119(1), 335–354. <https://doi.org/10.1002/2013JA019346>
- Tsyganenko, N. A., Andreeva, V. A., & Gordeev, E. I. (2015). Internally and externally induced deformations of the magnetospheric equatorial current as inferred from spacecraft data. *Annales Geophysicae*, 33(1), 1–11. <https://doi.org/10.5194/angeo-33-1-2015>
- Tsyganenko, N. A., Andreeva, V., Kubyshkina, M., Sitnov, M. I., & Stephens, G. K. (2021). Data-based modeling of the Earth's magnetic field. In *Magnetospheres in the solar system* (pp. 617–635). American Geophysical Union (AGU). <https://doi.org/10.1002/9781119815624.ch39>
- Tsyganenko, N. A., Andreeva, V. A., Sitnov, M. I., Stephens, G. K., Gjerloev, J. W., Chu, X., & Troshichev, O. A. (2021). Reconstructing substorms via historical data mining: Is it really feasible? *Journal of Geophysical Research: Space Physics*, 126(10), e2021JA029604. <https://doi.org/10.1029/2021JA029604>
- Tsyganenko, N. A., & Fairfield, D. H. (2004). Global shape of the magnetotail current sheet as derived from geotail and polar data. *Journal of Geophysical Research: Space Physics*, 109(A3). <https://doi.org/10.1029/2003JA010062>
- Tsyganenko, N. A., & Sitnov, M. I. (2005). Modeling the dynamics of the inner magnetosphere during strong geomagnetic storms. *Journal of Geophysical Research: Space Physics*, 110(A3). <https://doi.org/10.1029/2004JA010798>
- Tsyganenko, N. A., & Sitnov, M. I. (2007). Magnetospheric configurations from a high-resolution data-based magnetic field model. *Journal of Geophysical Research: Space Physics*, 112(A6). <https://doi.org/10.1029/2007JA012260>
- Vassiliadis, D. (2006). Systems theory for geospace plasma dynamics. *Reviews of Geophysics*, 44(2). <https://doi.org/10.1029/2004RG000161>
- Vassiliadis, D., Klimas, A., & Baker, D. (1999). Models of D_{sc} geomagnetic activity and of its coupling to solar wind parameters. *Physics and Chemistry of the Earth—Part C: Solar, Terrestrial & Planetary Science*, 24(1), 107–112. [https://doi.org/10.1016/S1464-1917\(98\)00016-6](https://doi.org/10.1016/S1464-1917(98)00016-6)
- Vassiliadis, D., Klimas, A. J., Baker, D. N., & Roberts, D. A. (1995). A description of the solar wind-magnetosphere coupling based on nonlinear filters. *Journal of Geophysical Research: Space Physics*, 100(A3), 3495–3512. <https://doi.org/10.1029/94JA02725>
- Verleyen, M., & François, D. (2005). The curse of dimensionality in data mining and time series prediction. In J. Cabestany, A. Prieto, & F. Sandoval (Eds.), *Computational intelligence and bioinspired systems* (pp. 758–770). Springer Berlin Heidelberg.
- Wang, C.-P., Lyons, L. R., Nagai, T., & Samson, J. C. (2004). Midnight radial profiles of the quiet and growth-phase plasma sheet: The geotail observations. *Journal of Geophysical Research: Space Physics*, 109(A12). <https://doi.org/10.1029/2004JA010590>
- Wettschereck, D., Aha, D. W., & Mohri, T. (1997). A review and empirical evaluation of feature weighting methods for a class of lazy learning algorithms. *Artificial Intelligence Review*, 11(1), 273–314. <https://doi.org/10.1023/A:1006593614256>

- Williams, T., Shulman, S., Ottenstein, N., Palmer, E., Riley, C., Letourneau, S., & Godine, D. (2020). Operational techniques for dealing with long eclipses during the MMS extended mission. In *2020 IEEE Aerospace Conference* (pp. 1–12). <https://doi.org/10.1109/AERO47225.2020.9172276>
- Xiao, C. J., Wang, X. G., Pu, Z. Y., Zhao, H., Wang, J. X., Ma, Z. W., et al. (2006). In situ evidence for the structure of the magnetic null in a 3-D reconnection event in the Earth's magnetotail. *Nature Physics*, *2*(7), 478–483. <https://doi.org/10.1038/nphys342>
- Yoon, P. H., & Lui, A. T. Y. (2005). A class of exact two-dimensional kinetic current sheet equilibria. *Journal of Geophysical Research: Space Physics*, *110*(A1). <https://doi.org/10.1029/2003JA010308>